



1 **PM<sub>2.5</sub> concentrations based on near-surface visibility at 4011 sites in the Northern**  
2 **Hemisphere from 1959 to 2022**

3 Hongfei Hao<sup>1</sup>, Kaicun Wang<sup>2</sup>, Guocan Wu<sup>1</sup>, Jianbao Liu<sup>2</sup>, Jing Li<sup>3</sup>

4 <sup>1</sup>Global Change and Earth System Science, Faculty of Geographical Science, Beijing Normal  
5 University, Beijing 100875, China

6 <sup>2</sup>Institute of Carbon Neutrality, Sino French Institute of Earth System Science, College Urban and  
7 Environmental Sciences, Peking University, Beijing 100871, China

8 <sup>3</sup>Institute of Carbon Neutrality, Sino French Institute of Earth System Science, Department of  
9 Atmospheric and Oceanic Sciences, School of Physics, Peking University, Beijing 100871, China

10 Corresponding Author: Email: [kcwang@pku.edu.cn](mailto:kcwang@pku.edu.cn)

11 **Abstract**

12 Long-term PM<sub>2.5</sub> data are needed to study the atmospheric environment, human health, and climate  
13 change. PM<sub>2.5</sub> measurements are sparsely distributed and of short duration. In this study, daily PM<sub>2.5</sub>  
14 concentrations are estimated from 1959 to 2022 using a machine learning method at 4011 terrestrial  
15 sites in the Northern Hemisphere based on hourly atmospheric visibility data, which are extracted  
16 from the Meteorological Terminal Aviation Routine Weather Report (METAR). PM<sub>2.5</sub> monitoring is  
17 the target of machine learning, and atmospheric visibility and other related variables are the inputs.  
18 The training results show that the slope between the estimated PM<sub>2.5</sub> concentration and the  
19 monitored PM<sub>2.5</sub> concentration is  $0.946 \pm 0.0002$  within the 95% confidence interval (CI), the  
20 coefficient of determination ( $R^2$ ) is 0.95, the root mean square error (RMSE) is  $7.0 \mu\text{g}/\text{m}^3$ , and the  
21 mean absolute error (MAE) is  $3.1 \mu\text{g}/\text{m}^3$ . The test results show that the slope between the predicted  
22 PM<sub>2.5</sub> concentration and the monitored PM<sub>2.5</sub> concentration is  $0.862 \pm 0.0010$  within a 95% CI, the  
23  $R^2$  is 0.80, the RMSE is  $13.5 \mu\text{g}/\text{m}^3$ , and the MAE is  $6.9 \mu\text{g}/\text{m}^3$ . The multiyear mean PM<sub>2.5</sub>  
24 concentrations from 1959 to 2022 in the United States, Canada, Europe, China, and India are  $11.2$   
25  $\mu\text{g}/\text{m}^3$ ,  $8.2 \mu\text{g}/\text{m}^3$ ,  $20.1 \mu\text{g}/\text{m}^3$ ,  $51.3 \mu\text{g}/\text{m}^3$  and  $88.6 \mu\text{g}/\text{m}^3$ , respectively. PM<sub>2.5</sub> is low and continues  
26 to decrease from 1959 to 2022. PM<sub>2.5</sub> in the United States increases slightly at a rate of  $0.38$   
27  $\mu\text{g}/\text{m}^3/\text{decade}$  from 1959 to 1990 and decreases at a rate of  $-1.32 \mu\text{g}/\text{m}^3/\text{decade}$  from 1991 to 2022.  
28 Trends in Europe are positive ( $5.69 \mu\text{g}/\text{m}^3/\text{decade}$ ) from 1959 to 1972 and negative ( $-1.91$   
29  $\mu\text{g}/\text{m}^3/\text{decade}$ ) from 1973 to 2022. Trends in China and India are increasing ( $3.04$  and  $3.35$   
30  $\mu\text{g}/\text{m}^3/\text{decade}$ , respectively) from 1959 to 2012 and decreasing ( $-38.82$  and  $-42.84 \mu\text{g}/\text{m}^3/\text{decade}$ ,  
31 respectively) from 2013 to 2022. The dataset is available at National Tibetan Plateau / Third Pole  
32 Environment Data Center (<https://doi.org/10.11888/Atmos.tpdc.301127>) (Hao et al., 2024).

33 **Keywords**

34 Fine particulate matter; PM<sub>2.5</sub>; Visibility; Machine learning; Dataset.

35 **1 Introduction**

36 Fine particulate matter (PM<sub>2.5</sub>) refers to particulate matter suspended in air with an aerodynamic  
37 diameter of less than 2.5 micrometers. PM<sub>2.5</sub> has various shapes and is composed of complex  
38 components, such as inorganic salts (e.g., sulfate, nitrate, and ammonium), as well as organic carbon



39 and elemental carbon, metallic elements, and organic compounds (Chen et al., 2020; Fan et al.,  
40 2021).  $PM_{2.5}$  can be emitted directly into the atmosphere (Viana et al., 2008; Zhang et al., 2019) and  
41 generated through photochemical reactions and transformations (Guo et al., 2014).  $PM_{2.5}$  exhibits  
42 high concentrations near emission sources, which gradually decreases with distance. Due to the  
43 small size and longer life span of  $PM_{2.5}$  compared with coarse particulate matter, it can be  
44 transported over long distances by atmospheric movements, leading to wide-ranging impacts.  
45 Studies indicate that regional transport contributes significantly to local  $PM_{2.5}$  (Wang et al., 2014;  
46 Chen et al., 2020).

47  $PM_{2.5}$  reduces atmospheric visibility and facilitates the formation of fog and haze conditions (Fan  
48 et al., 2021). Direct and indirect effects on solar radiation in the atmosphere (Albrecht, 1989;  
49 Ramanathan et al., 2001; Bergstrom et al., 2007; Chen et al., 2022) alter the energy balance and the  
50 number of condensation nuclei, thereby influencing atmospheric circulation and the water cycle  
51 (Wang et al., 2012; Liao et al., 2015; Samset et al., 2019; Li et al., 2022).

52  $PM_{2.5}$  is also known as respirable particulate matter. Due to its complex composition,  $PM_{2.5}$  may  
53 carry toxic substances that can significantly impair human health. The World Health Organization  
54 states explicitly that  $PM_{2.5}$  is more harmful than coarse particles, and long-term exposure to high  
55  $PM_{2.5}$  concentrations increases the risk of respiratory diseases, cardiovascular diseases, and lung  
56 cancer (Lelieveld et al., 2015), regardless of a country's development status. A Global Burden of  
57 Diseases study revealed that exposure to environmental  $PM_{2.5}$  causes thousands of deaths and  
58 millions of lung diseases annually (Chafe et al., 2014; Kim et al., 2015; Cohen et al., 2017).

59  $PM_{2.5}$  is an important parameter for assessing particulate matter pollution and air quality (Wang et  
60 al., 2012).  $PM_{2.5}$  can lead to soil acidification, water pollution, disruption of plant respiration, and  
61 ecological degradation (Wu and Zhang, 2018; Liu et al., 2019). Due to globalization and economic  
62 integration, preventing and controlling particulate matter pollution is a challenge at city, country  
63 and global scales.

64 Therefore, long-term  $PM_{2.5}$  data are needed for studies on the environment, human health, and  
65 climate change. At present, ground-based measurements, chemical models, and estimations of  
66 alternatives are the primary sources of  $PM_{2.5}$  data.

67 Ground-based measurements are the most effective means to measure  $PM_{2.5}$ .  $PM_{2.5}$  monitoring has  
68 been ongoing since the 1990s in North America and Europe (Van Donkelaar et al., 2010), and large-  
69 scale  $PM_{2.5}$  monitoring has been implemented in other regions since 2000, including China in 2013  
70 (Liu et al., 2017). As a result, the records for  $PM_{2.5}$  are short, with only a few years of data available  
71 in many countries. The scarcity of  $PM_{2.5}$  measurements makes it challenging to provide long-term  
72 historical data for research.

73 Reanalysis datasets provide estimates of long-term particulate matter concentrations. The Modern-  
74 Era Retrospective Analysis for Research and Applications version 2 (MERRA-2) is a reanalysis  
75 dataset from NASA that uses the Goddard Earth Observing System version 5 (GEOS-5), which has  
76 provided global  $PM_{2.5}$  data since 1980 (Buchard et al., 2015; Buchard et al., 2016; Buchard et al.,  
77 2017; Gelaro et al., 2017; Sun et al., 2019). The MERRA-2 surface  $PM_{2.5}$  assessment results are  
78 more consistent between observations located in rural areas, as cities and suburban areas are affected  
79 by high local emissions that do not represent the estimated grid average. Due to the lack of nitrate



80 and low organic carbon emissions in GOCART, there is a difference in the total amount of  $PM_{2.5}$   
81 during winter in the western United States, and sea salt aerosols are overestimated (Buchard et al.,  
82 2017). Another reanalysis dataset is the Copernicus Atmosphere Monitoring Service (CAMS) global  
83 reanalysis, which is a global reanalysis dataset of the atmospheric composition produced by the  
84 European Centre for Medium-Range Weather Forecasts (ECMWF) and has provided  $PM_{2.5}$  data  
85 since 2003 (Che et al., 2014; Inness et al., 2019). The validation of  $PM_{2.5}$  for CAMS shows severe  
86 overestimations in some areas (Ali et al., 2022; Jin et al., 2022). Although reanalysis provides long-  
87 term  $PM_{2.5}$  data, the uncertainty in emission inventories increases the uncertainty in  $PM_{2.5}$ , which  
88 remains challenging (Granier et al., 2011).

89 Many studies have employed statistical methods, machine learning, and deep learning methods to  
90 estimate  $PM_{2.5}$  concentrations based on aerosol optical depth (AOD). Van Donkelaar et al. (2021)  
91 utilized satellite AOD, chemical transport models, and ground-level measurements of AOD to  
92 estimate monthly  $PM_{2.5}$  concentrations and their uncertainties over global land from 1998 to 2019,  
93 and there are several related studies (Van Donkelaar et al., 2010; Boys et al., 2014; Van Donkelaar  
94 et al., 2015; Van Donkelaar et al., 2016; Hammer et al., 2020). Many studies have been conducted  
95 at the regional scale, such as in the United States (Beckerman et al., 2013), China (Wei et al., 2019b;  
96 Xue et al., 2019; Wei et al., 2020a; He et al., 2021; Wei et al., 2021), and India (Mandal et al., 2020).  
97 Although the  $PM_{2.5}$  data derived from satellite retrievals have high spatial coverage, the temporal  
98 range depends entirely on the satellite retrievals. The estimation of  $PM_{2.5}$  based on satellite products  
99 is also limited by bright surfaces, cloud conditions (Wei et al., 2019a) and resolution (Nagaraja Rao  
100 et al., 1989; Hsu et al., 2017).

101 Another alternative for estimating  $PM_{2.5}$  concentrations is the atmospheric horizontal visibility,  
102 which is the maximum distance at which observers with normal visual acuity can discern target  
103 contours under current weather conditions. In addition to manual observations, automated visibility  
104 measurements were implemented early, typically relying on the aerosol scattering principle (Wang  
105 et al., 2009; Zhang et al., 2020). Visibility and  $PM_{2.5}$  are measurements of near-surface aerosols.  
106 They describe atmospheric transparency and are used to describe atmospheric pollution. Long-term  
107 visibility records have been used to quantify long-term aerosol properties (Molnár et al., 2008; Wang  
108 et al., 2009; Zhang et al., 2017; Zhang et al., 2020). Visibility observation stations are densely  
109 distributed across the country. Compared to satellite-retrieved AOD data, visibility observations  
110 have longer historical records dating back to the early 20th century (Noaa et al., 1998; Boers et al.,  
111 2015), are not affected by cloud interference and provide continuous measurements.

112 Visibility has been used as a proxy for  $PM_{2.5}$  (Huang et al., 2009) and to estimate  $PM_{2.5}$  (Liu et al.,  
113 2017; Li et al., 2020; Singh et al., 2020). Singh et al. (2020) analyzed the air quality in East Africa  
114 from 1974 to 2018 using visibility data. Liu et al. (2017) developed a statistical model and utilized  
115 ground-level visibility data to estimate long-term  $PM_{2.5}$  concentrations in China from 1957 to 1964  
116 and 1973 to 2014. Gui et al. (2020) proposed a method to establish a virtual ground observation  
117 network for  $PM_{2.5}$  in China using extreme gradient boosting modeling in 2018. Zeng et al. (2021)  
118 used LightGBM to establish a virtual network for hourly  $PM_{2.5}$  concentrations in China in 2017.  
119 Zhong et al. (2021; 2022) used LightGBM to predict 6-hour  $PM_{2.5}$  concentrations based on visibility,  
120 temperature, and relative humidity in China from 1960 to 2020. Meng et al. (2018) utilized a random  
121 forest model to estimate the daily  $PM_{2.5}$  components in the United States from 2005 to 2015. These  
122 studies have provided various methods for estimating  $PM_{2.5}$  using visibility data. However, some



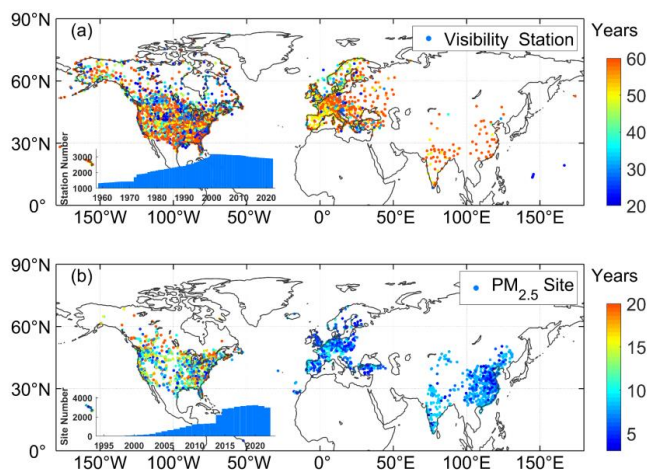
123 have focused on only methodological innovations without providing long-term trends in  $PM_{2.5}$ .  
124 Other studies offer long-term trends, but the primary focus was at urban and national scales. There  
125 are few studies on long-term and high-temporal-resolution  $PM_{2.5}$  at the global scale or across  
126 different countries.

127 This study uses a convenient, accurate, and easily understandable machine learning approach to  
128 estimate daily  $PM_{2.5}$  concentrations based on visibility at 4,011 land-based sites from 1959 to 2022.  
129 We also provide the long-term trends and characteristics of  $PM_{2.5}$  in different regions. The  $PM_{2.5}$   
130 dataset provides support for climate change, human health, and pollution control research. First, we  
131 build a machine learning model and then analyze the importance of the variables. Second, we  
132 evaluate the model's performance and predictive ability. Third, we discuss the errors and limitations  
133 of the dataset. Fourth, we compare the estimated  $PM_{2.5}$  with the other datasets. Finally, we analyze  
134 the spatial-temporal distributions of  $PM_{2.5}$ .

## 135 2 Data and methods

### 136 2.1 Study Area

137 The study area includes Canada, the United States, Europe, China, and India in the Northern  
138 Hemisphere. The distributions of visibility stations (a) and the  $PM_{2.5}$  monitoring sites (b) in each  
139 region are shown in Figure 1. The number of visibility stations is 3177, and a total of 4011  $PM_{2.5}$   
140 monitoring sites are selected for this study, with 1110 sites in the United States, 304 sites in Canada,  
141 834 sites in Europe, 1557 sites in China, and 206 sites in India.



142

143 **Figure 1** Study area and the distribution of visibility stations from 1959 to 2022 (a) and  $PM_{2.5}$   
144 monitoring sites from 1995 to 2022 (b). The color of marker (circle) represents that the length of  
145 the observation record of visibility and  $PM_{2.5}$  observations. The bar chart shows the number of  
146 visibility stations and  $PM_{2.5}$  monitoring sites per year. The number of visibility stations is 3177. The  
147 number of  $PM_{2.5}$  sites is 4011 in this study (1110 in the United States, 304 in Canada, 834 in Europe,  
148 1557 in China, and 206 in India).

### 149 2.2 $PM_{2.5}$ Data



### 150 **2.2.1 PM<sub>2.5</sub> Data in the United States**

151 The hourly PM<sub>2.5</sub> data for the United States from 1998 to 2022 are sourced from the Air Data System  
152 (AQS), which are available at <https://www.epa.gov/aqs>. The AQS provides PM<sub>2.5</sub> mass monitoring  
153 and routine chemical speciation data and contains other ambient air pollution data collected by the  
154 Environmental Protection Agency (EPA), state, local, and tribal air pollution control agencies from  
155 thousands of monitors, comprising the Federal Reference Method (FRM) and Federal Equivalent  
156 Method (FEM). The primary purpose of both methods is to assess compliance with the PM<sub>2.5</sub>  
157 National Ambient Air Quality Standards (NAAQS). FRMs include in-stack particulate filtration,  
158 and FEMs include beta-attenuation monitoring, very sharp cut cyclones, and tapered element  
159 oscillating microbalances (TOEMs). The measurement precision is  $\pm (1\sim 2) \mu\text{g}/\text{m}^3$  (hour) (Gilliam  
160 and Hall, 2016). The TEOM and beta-attenuation are automatic and near real-time monitoring  
161 methods. The TEOM, which is based on gravity, measures the mass of particles collected on filters  
162 by monitoring the frequency changes in tapered elements. The beta-attenuation method uses beta-  
163 ray attenuation and particle mass to measure the PM<sub>2.5</sub> concentration. In this study, we use two PM<sub>2.5</sub>  
164 measurement methods, FRM/FEM (88101) and non-FRM/FEM (88502). The 88502 monitors are  
165 “FRM-like” but are not used for regulatory purposes. Both the 88101 and 88502 monitors are used  
166 for reporting daily Air Quality Index values.

167 We set the conditions that each PM<sub>2.5</sub> monitoring event have a minimum of 3 years and more than  
168 1000 days of overlapping records with nearby visibility stations. A total of 1110 sites in the United  
169 States are selected for this study.

### 170 **2.2.2 PM<sub>2.5</sub> Data in Canada**

171 The hourly PM<sub>2.5</sub> data for Canada from 1995 to 2022 are sourced from the National Air Pollution  
172 Surveillance (NAPS) program, which are available at <https://www.canada.ca>. The NAPS program  
173 is a collaborative effort between the Environment and Climate Change Canada and provincial,  
174 territorial, and regional governments and is the primary source of environmental air quality data.  
175 Since 1984, PM<sub>2.5</sub> concentrations have been measured in Canada using a dichotomous sampler.  
176 Continuous or real-time particle monitoring began in the NAPS network in 1995 using TEOM and  
177 beta-attenuation monitoring (Demerjian, 2000). The samples are supplemented by EPA FRM  
178 samples obtained after 2009 (Dabek-Zlotorzynska et al., 2011). The number of instruments is  
179 growing rapidly, with 410 sites in 2022. A total of 304 PM<sub>2.5</sub> monitoring sites in Canada are selected  
180 for this study.

### 181 **2.2.3 PM<sub>2.5</sub> Data in Europe**

182 The hourly PM<sub>2.5</sub> data for Europe from 1998 to 2012 are obtained from the AirBase database, which  
183 is available at <https://european-union.europa.eu>. The hourly PM<sub>2.5</sub> verified data (E1a) from 2013 to  
184 2022 are obtained from the AirQuality database, which is available at <https://www.eea.europa.eu>.  
185 AirBase is maintained by the European Environment Agency (EEA) through its European Topic  
186 Center on Air Pollution and Climate Change Mitigation. Airbase contains air quality monitoring  
187 data and information submitted by participating countries throughout Europe. After the Air Quality  
188 Directive 2008/50/EC was enforced, the PM<sub>2.5</sub> data began to be stored in AirQuality database. The  
189 main monitoring methods for PM<sub>2.5</sub> include TEOM and beta attenuation (Green and Fuller, 2006;  
190 Chow et al., 2008). The sites are distributed across rural, rural-near city, rural-regional, rural-remote,



191 suburban, and urban areas. We merge the two datasets with the same site identifiers, and 834 sites  
192 in Europe are selected for this study.

#### 193 **2.2.4 PM<sub>2.5</sub> Data in China**

194 The hourly PM<sub>2.5</sub> data for China from 2014 to 2022 are obtained from the China National  
195 Environmental Monitoring Center, which are available at <https://www.cnemc.cn>. China established  
196 air quality monitoring in 1980; 74 cities were the first to publicly release real-time PM<sub>2.5</sub> in 2013,  
197 and there were more than 1800 air quality observation sites as of 2000 (Su et al., 2022). PM<sub>2.5</sub>  
198 concentrations are measured using the TEOM and beta-attenuation method (Zhao et al., 2016b;  
199 Miao and Liu, 2019). According to the China Environmental Protection Standards, instrument  
200 maintenance, data transmission, data assurance and quality control ensure the reliability of PM<sub>2.5</sub>  
201 concentration measurements. The uncertainty in the PM<sub>2.5</sub> mass concentration is <5 µg/m<sup>3</sup> (Pui et  
202 al., 2014). In this study, a total of 1110 PM<sub>2.5</sub> monitoring sites are selected.

#### 203 **2.2.5 PM<sub>2.5</sub> Data in India**

204 The hourly PM<sub>2.5</sub> data for India from 2010 to 2022 are obtained from the Central Pollution Control  
205 Board (CPCB), which are available at <https://app.cpcbcr.com>. The Air (Prevention and Control of  
206 Pollution) Act of 1981 was enacted by the Central Pollution Control Board (CPCB) of the Ministry  
207 of Environment, Forest and Climate Change (MoEFCC). A standard of 60 µg/m<sup>3</sup> PM<sub>2.5</sub>  
208 concentration over 24 hours was added in 2009. The methods used by the Indian National Ambient  
209 Air Quality Standards (NAAQS) for PM<sub>2.5</sub> and related component measurements include the TEOM,  
210 FRM and FEM (Pant et al., 2019). The measurement precision is ± (1-2) µg/m<sup>3</sup> (hour). The National  
211 Air Quality Monitoring Programme (NAMP) is a key air quality monitoring programme employed  
212 by the Government of India, which is managed by the CPCB in coordination with the State Pollution  
213 Control Boards (SPCBs) and UT (union territory) Pollution Control Committees (PCCs). There  
214 were 703 PM<sub>2.5</sub> monitoring stations as of 2018. Most of these stations (residential and industrial)  
215 are located in urban areas, and others are located sparsely in rural areas. A total of 206 PM<sub>2.5</sub>  
216 monitoring sites are selected for this study.

#### 217 **2.3 Visibility and Meteorological Data**

218 The hourly meteorological data from 1959 to 2022 are collected from airport weather observations,  
219 which are available at <https://www.weather.gov/asos>. Automated observation minimizes the errors  
220 associated with human involvement in data collection, processing, and transmission. The data are  
221 extracted from the Meteorological Terminal Aviation Routine Weather Report (METAR). The World  
222 Meteorological Organization (WMO) sets guidelines for METAR reports, including report format,  
223 encoding, observation instruments and methods, data accuracy, and consistency. These requirements  
224 ensure the consistency and comparability of METAR reports globally. Visibility is a quantity that  
225 describes the atmospheric transparency, usually observed by automated sensors (scattering and  
226 transmission). More than 1000 stations are from the Automated Surface Observing System (ASOS)  
227 in the United States, and other data are sourced from airport reports worldwide. The forward-scatter  
228 visibility sensors at a wavelength of 550 nm for ASOS are consistent with the National Weather  
229 Service of the United States standard transmissometer, with more than 80% of the data within the  
230 limit of ±0.4 km when visibility is less than 2 km (Noaa et al., 1998).

231 Visibility is an essential variable employed in this study, as research has shown that its reciprocal is



232 directly proportional to the aerosol extinction coefficient (Wang et al., 2009), which is closely  
233 related to the  $PM_{2.5}$  concentration. Considering that temperature, wind speed, wind direction,  
234 humidity, and precipitation are factors that impact particle dispersion, particle growth, and  
235 secondary generation influenced by humidity, as well as the cleansing effect of precipitation (Zhang  
236 et al., 2020), temperature, dew point temperature, temperature-dew point difference, relative  
237 humidity, sea-level pressure, wind speed and direction, precipitation, and sky conditions are also  
238 employed in this study.

#### 239 **2.4 Data Preprocessing**

240 The following data preprocessing steps are performed: remove the records with missing visibility,  
241 temperature, dew point temperature, temperature-dew point difference, relative humidity, sea-level  
242 pressure, wind speed, and wind direction data and remove records with hourly precipitation greater  
243 than 0.1 mm, sky conditions marked as 'VV', and relative humidity greater than 90%. Since  $PM_{2.5}$   
244 exhibits hygroscopic growth, we calculated the dry visibility for relative humidity values between  
245 30% and 90% (Yang et al., 2021).

$$246 \quad \mathit{VISD} = \mathit{VIS} / (0.26 + 0.4285 * \log(100 - \mathit{RH}))$$

247 where VIS is the visibility, RH is the relative humidity, and VISD is the dry visibility.

248 The maximum hourly  $PM_{2.5}$  concentration is set to  $1000 \mu\text{g}/\text{m}^3$ . At least three hourly daily records  
249 are needed. The harmonic mean is used to calculate the daily VIS and daily VISD because it can  
250 better capture rapid weather changes and enhance daily representativeness (Noaa et al., 1998). The  
251 arithmetic average is used for other variables.

#### 252 **2.5 Data for Comparison**

253 In this study, our data are compared with other datasets, including two  $PM_{2.5}$  datasets based on  
254 satellite AOD data and two reanalysis datasets.

##### 255 **2.5.1 ACAG Dataset**

256 The monthly global  $PM_{2.5}$  dataset (version V5.GL.04) from 1980 to 2022, with a spatial resolution  
257 of  $0.1^\circ$ , is available from the Atmospheric Composition Analysis Group (ACAG) of Washington  
258 University in St. Louis (<https://sites.wustl.edu/acag/datasets/surface-pm2-5/>) (Van Donkelaar et al.,  
259 2021). The ACAG  $PM_{2.5}$  concentrations are estimated based on satellite (MODIS, VIIRS, MISR  
260 and SeaWiFS) AOD and global vertical aerosol profiles from the Cloud-Aerosol Lidar and Infrared  
261 Pathfinder Satellite Observation (CALIPSO) satellites. The AOD of GEOS-Chem is used to  
262 simulate the spatiotemporally varying geophysical relationship with  $PM_{2.5}$ . Ground-based  $PM_{2.5}$   
263 values are incorporated at a monthly timescale using geographically weighted regression (Van  
264 Donkelaar et al., 2016; Hammer et al., 2020; Van Donkelaar et al., 2021). The coefficients of  
265 determination ( $R^2$ ) for the monthly mean and monitor-based  $PM_{2.5}$  concentrations are 0.86 (January),  
266 0.81 (April), 0.72 (July), and 0.78 (October). The  $R^2$  with WHO-collocated monitors is between  
267 0.88 and 0.93. The EMSE is between 8 and  $13.3 \mu\text{g}/\text{m}^3$ .

##### 268 **2.5.2 CHAP Dataset**

269 The monthly  $PM_{2.5}$  dataset of China High Air Pollutants (CHAP) from 2000 to 2021 is a product  
270 with coverage over China, with a spatial resolution of 1 km, which is available at



271 <https://zenodo.org/records/6398971>. The CHAP PM<sub>2.5</sub> concentration is estimated based on the  
272 MODIS Collection 6 MAIAC AOD product and meteorological variables, surface conditions,  
273 pollutant emissions, and population distributions using a space-time extra-trees model. The R<sup>2</sup> and  
274 RMSE of the monthly PM<sub>2.5</sub> concentration are 0.92-0.94 and ~5.1-10.0 µg/m<sup>3</sup>, respectively, from  
275 2013 to 2018 (Wei et al., 2020b; Wei et al., 2021).

### 276 2.5.3 MERRA-2 Dataset

277 The monthly PM<sub>2.5</sub> dataset of Modern-Era Retrospective Analysis for Research and Applications  
278 version 2 (MERRA-2) from 1980 to 2022 is a NASA reanalysis dataset with a spatial resolution of  
279 0.5×0.625° and uses the Goddard Earth Observing System version 5 (GEOS-5) coupled to the  
280 Goddard Chemistry Aerosol Radiation and Transport (GOCART) model, which is available at  
281 <https://gmao.gsfc.nasa.gov>. The aerosol data of GOCART include dust, sea salt, sulfate, black  
282 carbon, and organic carbon, and there are 72 vertical layers from the surface to more than 80 km  
283 altitude. MERRA-2 PM<sub>2.5</sub> is a dataset produced by the GEOS-5 atmospheric model and data  
284 assimilation system and the three-dimensional variational data analysis (3DVAR) Grid-point  
285 Statistical Interpolation (GSI) meteorological analysis scheme (Randles et al., 2017). In the aerosol  
286 model (GOCART), a SO<sub>2</sub> emission database of volcanic material for secondary sources is included.  
287 Aerosol hygroscopic growth depends on the simulated relative humidity. The monthly scale biomass  
288 burning inventory is from RETROv2 from 1980 to 1996; the monthly SO<sub>2</sub>, SO<sub>4</sub>, POM, and BC  
289 emissions are from GFEDv3.1 from 1997 to 2009; and the daily scale data are from QFED 2.4-r6  
290 after 2010. The annual anthropogenic SO<sub>2</sub> is from EDGARv4.2 between 100 and 500 m above the  
291 surface from 1980 to 2008. The annual Anthropogenic SO<sub>4</sub>, BC, and POM concentrations are  
292 obtained from AeroCom Phase II from 1980 to 2006. In assimilation systems, satellite AOD  
293 retrievals are used, including AVHRR (over the oceans) from 1998 to 2002, MISR from 2000 to  
294 2014, MODIS Aqua since 2002, and MODIS Terra since 2000 (Buchard et al., 2017; Randles et al.,  
295 2017). The direct observations of the AOD AERONET station from 1999 to 2014 are also  
296 assimilated.

297 The surface PM<sub>2.5</sub> concentration in MERRA-2 can be computed using the concentrations of black  
298 carbon [BC], organic carbon [OC], dust [DUST<sub>2.5</sub>], sea salt [SS<sub>2.5</sub>], and sulfate [SO<sub>4</sub>] (Provençal et  
299 al., 2017) and is expressed as follows (please refer to  
300 <https://gmao.gsfc.nasa.gov/reanalysis/MERRA-2/FAQ/#Q4>):

$$301 \text{ [PM}_{2.5}\text{]} = \text{ [DUST}_{2.5}\text{]} + \text{ [SS}_{2.5}\text{]} + \text{ [BC]} + 1.6 \times \text{ [OC]} + 1.375 \times \text{ [SO}_4\text{]}.$$

302 In this study, we conduct spatiotemporal matching between MERRA-2 PM<sub>2.5</sub> and the estimated  
303 PM<sub>2.5</sub>.

### 304 2.5.4 CAMS Dataset

305 The Copernicus Atmosphere Monitoring Service (CAMS) reanalysis is the latest global reanalysis  
306 dataset of atmospheric composition produced by the European Centre for Medium-Range Weather  
307 Forecasts (ECMWF). We use the single-level monthly PM<sub>2.5</sub> product from the CAMS reanalysis  
308 from 2003 to 2022, which is available at  
309 <https://ads.atmosphere.copernicus.eu/cdsapp#!/dataset/cams-global-reanalysis-eac4>. The resolution  
310 is 0.75°. The CAMS reanalysis builds on the experience gained during the earlier Monitoring  
311 Atmospheric Composition and Climate (MACC) reanalysis and CAMS interim reanalysis (Inness





312 et al., 2019). The ECMWF's Integrated Forecast System (IFS) aerosol and chemistry modules are  
313 applied, and more details on the modules are provided in (2015). The data at 60 model levels are  
314 interpolated to 25 pressure levels. Anthropogenic emissions are from the MACCity inventory from  
315 1960 to 2010 (Granier et al., 2011). The emissions of anthropogenic SOAs are estimated from  
316 MACCity CO emissions. The monthly biogenic emissions of the chemical species are from  
317 MEGAN2.1 (Guenther et al., 2006). The natural NO<sub>2</sub> emissions from soils and oceans are obtained  
318 from the Precursors of Ozone and Their Effects in the Troposphere (POET) database for 2000. Daily  
319 biomass burning emissions are from the Global Fire Assimilation System version 1.2 (GFASv1.2)  
320 (Kaiser et al., 2012). More details regarding emissions are provided in Granier (2011). The  
321 incremental 4D-Var data assimilation system is used for the CAMS reanalysis, and the total aerosol  
322 mixing ratio of the single species is derived from the assimilation of satellite retrievals (Benedetti  
323 et al., 2009). The AODs from satellite retrievals are assimilated, including those from AATSR  
324 Envisat from 2002 to 2012 and those from MODIS Terra and Aqua since 2002. For additional  
325 information, please refer to Inness et al. (2019).

326 The surface PM<sub>2.5</sub> concentration is estimated by the air density [ $\rho$ ], sea salt [SS<sub>1,2</sub>], dust [DD<sub>1,2,3</sub>],  
327 nitrate [NI<sub>1,2</sub>], organic matter [OM], black carbon [BC], ammonium [AM], and sulfate [SO<sub>4</sub>] and is  
328 expressed as follows (Inness et al., 2019):

$$329 \text{ [PM}_{2.5}\text{]} = \rho \times ([\text{DD}_1] + [\text{DD}_2] + [\text{SS}_1/4.3] + [0.5 \times \text{SS}_2/4.3] + [0.7 \times (\text{AM} + \text{OM} + 0.7\text{NI}_1 + \text{SO}_4)] +$$
$$330 [\text{BC}] + 0.25 \times [\text{NI}_2]).$$

## 331 2.6 Decision Tree Regression

332 We employ decision tree regression using the CART algorithm (Teixeira, 2004) to estimate daily  
333 PM<sub>2.5</sub> concentrations. The key to decision tree regression is to find the optimal split variable and  
334 optimal split point. The optimal split point of the predictor is determined by the minimum mean  
335 squared error, which determines the optimal tree structure. Decision tree regression is a commonly  
336 used nonlinear machine learning method that partitions the feature space based on the mapping  
337 between feature attributes and response values, with each leaf node representing a specific output  
338 for each feature space region. It's ability to handle complex relationships with relatively few model  
339 parameters is advantageous, minimizing the risk of overfitting and enabling the prediction of  
340 continuous and categorical predictive variables.

341 The predictor includes 11 variables: the reciprocal of dry visibility (Vis\_Dry\_In), the reciprocal of  
342 visibility (Vis\_In), temperature (Temp), dew point temperature (Td), temperature-dew point  
343 difference (Temp-Td), relative humidity (RH), sea-level pressure (SLP), wind speed (WS), wind  
344 direction (WD), numerical time (DateTime) and daily record number (DailyObsNum). The response  
345 variable is the daily observed PM<sub>2.5</sub> concentration.

346 We randomly select 80% of the sample data to establish the decision tree regression model, and the  
347 remaining 20% of the sample data are used to test the model's predictive ability. To obtain a stable  
348 model, a 10-fold cross-validation method (Browne, 2000) is used to train the model.

## 349 2.7 Evaluation Metrics

### 350 2.7.1 Statistical Metrics

351 We use the root mean squared error (RMSE), mean absolute error (MAE), and correlation



352 coefficient ( $\rho$ ) as evaluation metrics to evaluate the model's performance and predictive ability. The  
 353 formulas are given as follows:

$$354 \quad MSE = \sqrt{\frac{1}{n} \sum_{i=1}^n (y_i - \hat{y}_i)^2}$$

$$355 \quad MAE = \frac{1}{n} \sum_{i=1}^n |y_i - \hat{y}_i|$$

$$356 \quad \rho = \frac{\sum_{i=1}^n (y_i - \bar{y})(\hat{y}_i - \bar{\hat{y}})}{\sqrt{\sum_{i=1}^n (y_i - \bar{y})^2 \sum_{i=1}^n (\hat{y}_i - \bar{\hat{y}})^2}}$$

357 where  $y_i$  and  $\bar{y}$  are the predicted value and the average of the predicted values.  $\hat{y}_i$  and  $\bar{\hat{y}}$  are  
 358 the target and the average of the target.  $i = 1, 2, \dots, n$ .  $n$  is the length of sample.

### 359 2.7.2 Partial Dependence

360 The importance of predictor variables is assessed via partial dependence. Partial dependence  
 361 represents the relationship between the individual predictive variable and the predicted response  
 362 (Friedman, 2001). By marginalizing the other variables, the expected response of the predicted  
 363 variable is calculated. All the partial dependences of the predicted response on the subset of  
 364 predicted variables are calculated. The calculation process of the partial dependency method is  
 365 described as follows:

366 The dataset of the predictor is  $X$ ,  $X = [X^1, X^2, \dots, X^n]$ , and  $n$  represents the number of predictive  
 367 factors. The complement of subset  $X^s$  is  $X^c$ , where  $X^s$  is a single variable in  $X$  and  $X^c$  is all  
 368 other variables in  $X$ . The predicted response  $f(x)$  depends on all variables in  $X$ , and it is expressed  
 369 as follows:

$$370 \quad f(x) = f(X^s, X^c)$$

371 The partial dependence of the predicted response to  $X^s$  is expressed as follows:

$$372 \quad f^s(X^s) = \int f(X^s, X^c) pC(X^c) dX^c$$

373 where  $pC(X^c)$  is the marginal probability of  $X^c$ , that is,  $pC(X^c) \approx \int f(X^s, X^c) dX^s$ . Assuming  
 374 that the likelihood for each observation is equal, the dependence between  $X^s$  and  $X^c$  and the  
 375 interactions of  $X^s$  and  $X^c$  in response are not strong. The partial dependence is shown below:

$$376 \quad f^s(X^s) \approx \frac{1}{N} \sum_{i=1}^N f(X^s, X_i^s)$$

377 where  $N$  is the number of observations and  $i$  represents the  $i$ th observation.

### 378 2.7.3 Mean Center



379 The mean center is a geostatistical method used to describe the average position of a set of  
380 geographical coordinates. It represents the central tendency of a set of geographical data and aids in  
381 understanding the overall distribution and trends in the dataset. The mean center of the PM<sub>2.5</sub>  
382 concentration shows the overall trend and variability in PM<sub>2.5</sub>. If the mean center is located at the  
383 edge of the dataset, the data distribution is dispersed. Conversely, if the mean center is located at  
384 the center of the dataset, the data distribution is concentrated. This may be relevant for aspects, such  
385 as population distribution, urban development, and economic activities. It is particularly helpful in  
386 understanding the spatial patterns of PM<sub>2.5</sub>. The expression is given as follows:

$$387 \quad x_{ct} = \frac{\sum_{i=1}^N c_i * x_i}{\sum_{i=1}^N c_i}$$

$$388 \quad y_{ct} = \frac{\sum_{i=1}^N c_i * y_i}{\sum_{i=1}^N c_i}$$

389 where  $x_{ct}$  and  $y_{ct}$  represent the longitude and latitude of the mean center, respectively, and  $c_i$   
390 represents the PM<sub>2.5</sub> concentration at the  $i$ -th site ( $x_i$ ,  $y_i$ ).

### 391 2.7.4 Standard Deviation Ellipse

392 The standard deviation ellipse (SDE) is used in statistics and geography to describe the variability  
393 and correlation of multivariate data. The SDE is calculated based on the mean and covariance matrix  
394 of the data (Gong, 2002). This variable shows the dispersion and correlation of the data across  
395 different dimensions. The center of the ellipse corresponds to the mean of the data, while the shape  
396 and size of the ellipse reflect the variability in the data in different directions.

397 We calculate the SDE using the locations and concentration measurements associated with the PM<sub>2.5</sub>  
398 points. The major axis of the ellipse indicates the primary direction of data variation. The shape and  
399 size of the ellipse reflect the spatial dispersion of the PM<sub>2.5</sub> concentration. A larger ellipse indicates  
400 greater variability in the PM<sub>2.5</sub> concentration distribution, while a smaller ellipse denotes a more  
401 concentrated distribution. A circular ellipse indicates little or weak spatial correlation among PM<sub>2.5</sub>  
402 concentrations. A flattened ellipse indicates a spatial correlation between PM<sub>2.5</sub> concentrations.

## 403 3. Results and Discussion

### 404 3.1 Evaluation of Variable Importance

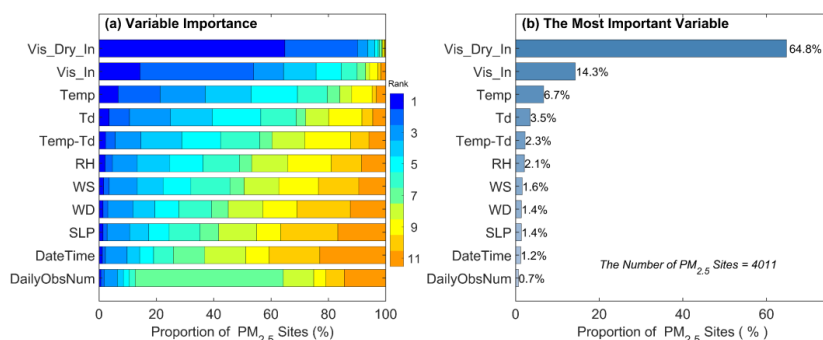
405 We analyze the influence of predictive variables over the predicted response. The predictive variable  
406 with the highest partial dependence value is the most important predictive variable in the model.  
407 The partial dependence of the predicted response on each predictive variable is calculated for every  
408 model. Figure 2 (a) shows the ranking results of the importance of all the predictive variables. The  
409 variable with the highest dependence on the predicted response is Vis\_Dry\_In, and the second  
410 highest dependence is Vis\_In. The dependence of the predicted response on Temp, Td, Temp-Td,  
411 RH, WS, and wind WD is moderate. The predictive variables with lower dependence include SLP,  
412 DateTime and DailyObsNum.

413 We count the frequency and proportion of the most important variables in all the models, as shown



414 in Figure 2 (b). `Vis_Dry_In` is the most important variable at 2600 sites, contributing 64.8%. `Vis_In`  
415 was the second most important variable at 575 sites, accounting for 14.3%. This finding indicates  
416 that visibility is the most crucial variable, with a percentage of 79.1%. `Temp` and `Td` contribute 6.7%  
417 and 3.5%, respectively. The contribution of other variables combined is 10.7%. The percentages of  
418 the second most important predictive variable are 25.4% for `Vis_In`, 39.6% for `Vis_Dry_In`, 14.6%  
419 for `Temp`, 7.1% for `Td` and 3.4% for `Temp-Td`. Among the three most important variables, the  
420 proportions of `Temp` and `Td` are 15.7% and 14.3%, respectively.

421 The results indicate a strong correlation between the  $PM_{2.5}$  concentration and visibility, as visibility  
422 can be considered an indicator of air quality without fog or precipitation. Meteorological factors  
423 influence the dispersion and deposition of  $PM_{2.5}$  (Gui et al., 2020; Zhong et al., 2022). Temperature  
424 and dew play secondary roles, and other meteorological predictive variables play lesser roles in the  
425 model. Although the number of daily records and time have the most negligible impacts on the  $PM_{2.5}$   
426 concentration in the model, they have significant impacts on the cyclical changes and daily  
427 representativeness of  $PM_{2.5}$  (Wang et al., 2012; Zhang et al., 2020).



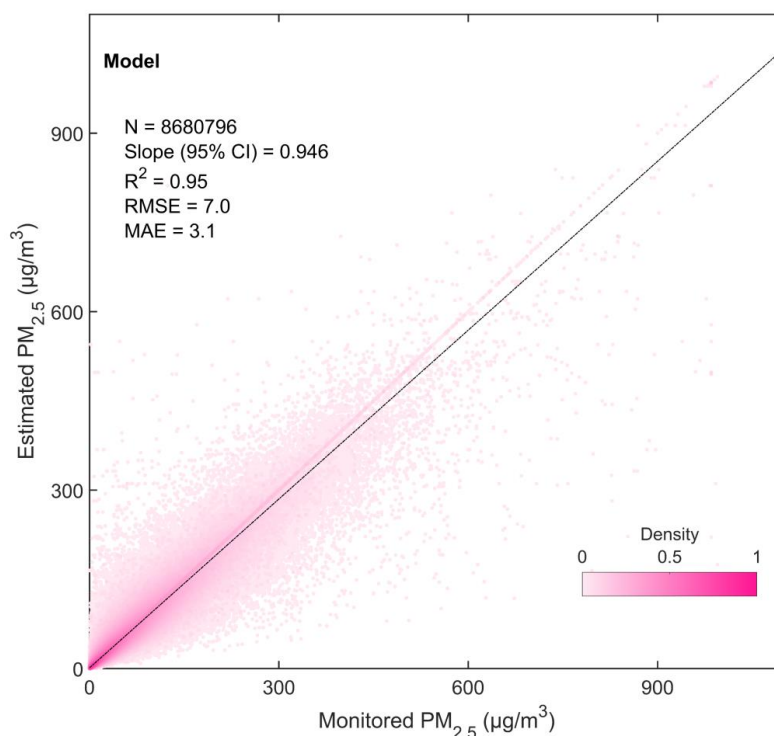
428

429 **Figure 2** The importance of predictive variables. The stacked bar (a) shows the importance rankings  
430 of the predictive variables ('rank=1' represents the most important variable). The bar (b) shows the  
431 percentage of the most important predictive variable. The predictive variables are the reciprocal of  
432 dry visibility (`Vis_Dry_In`), reciprocal of visibility (`Vis_In`), temperature (`Temp`), dew point  
433 temperature (`Td`), temperature-dew point difference (`Temp-Td`), relative humidity (`RH`), sea level  
434 pressure (`SLP`), wind speed (`WS`), wind direction (`WD`), numerical time (`DateTime`) and daily  
435 record number (`DailyObsNum`). The total number of  $PM_{2.5}$  sites is 4011.

### 436 3.2 Evaluation of Model Performance

#### 437 3.2.1 For All Data

438 We analyze the linear fitting relationship between all estimated and corresponding response values  
439 to evaluate the model's performance. Figure 3 shows the density scatter plot of the monitored  $PM_{2.5}$   
440 concentration (response values) and the estimated  $PM_{2.5}$  concentration (estimated values). There is  
441 a total of 8,680,796 data pairs for all the sites. The linear regression coefficient is  $0.946 \pm 0.0002$   
442 within the 95% confidence interval, the  $R^2$  is 0.95, the RMSE is  $7.0 \mu\text{g}/\text{m}^3$ , and the MAE is  $3.1$   
443  $\mu\text{g}/\text{m}^3$ .



444

445 **Figure 3** Density scatter plot (a) between estimated values (estimated  $PM_{2.5}$ ) and the corresponding  
446 response values (monitored  $PM_{2.5}$ ) at the daily scale. The dashed black line is the linear regression  
447 line.  $N$  is the length of the data pairs, and Slope is the linear regression coefficient within a 95%  
448 confidence interval (CI).  $R^2$  is the coefficient of determination, RMSE is the root mean square error,  
449 and MAE is the mean absolute error.

### 450 3.2.2 For the Site and Region Scales

451 We evaluate the model's performance using the RMSE, MAE, and  $\rho$  of the estimated and response  
452 values at the site and region scales. Figure 4 shows the spatial distribution (a-c) and frequency  
453 distribution (d-f) of the model's RMSE, MAE, and  $\rho$  at all sites. Table 1 lists the model's performance  
454 metrics for all sites and sites in the United States, Canada, Europe, China, and India.

455 For all sites, the average RMSE is  $7.42 \mu\text{g}/\text{m}^3$ , with a median of  $4.97 \mu\text{g}/\text{m}^3$ . The RMSE of 80% of  
456 the sites is less than  $11.95 \mu\text{g}/\text{m}^3$ . The ratio of the RMSE to the average  $PM_{2.5}$  concentration is 29.2%.  
457 The average MAE is  $4.01 \mu\text{g}/\text{m}^3$ , with a median of  $2.66 \mu\text{g}/\text{m}^3$ . The MAE is less than  $6.62 \mu\text{g}/\text{m}^3$   
458 for 80% of the sites. The MAE-to-mean ratio is 15.8%. The average  $\rho$  is 0.90, and the median is  
459 0.91. The  $\rho$  of 80% of the sites is greater than 0.87. Previous studies have shown that for  $PM_{2.5}$   
460 retrieved from daily visibility or satellite AOD data, the  $R^2$  range of the model is from 0.42 to 0.89,  
461 and the RMSE range is from  $9.59 \mu\text{g}/\text{m}^3$  to  $32.09 \mu\text{g}/\text{m}^3$  (Shen et al., 2016; Liu et al., 2017; Wei et  
462 al., 2019b; Gui et al., 2020; Li et al., 2021; Zhong et al., 2021). This finding indicates that our model



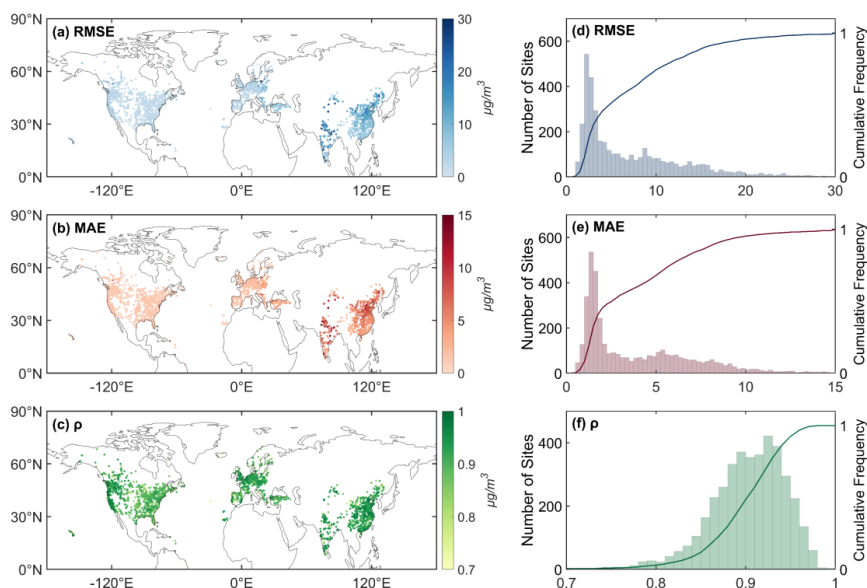
463 performs well at the daily scale.

464 At the regional scale, the average RMSE values for the United States, Canada, Europe, China, and  
465 India are 7.8, 2.86, 4.63, 11.62, and 18.73  $\mu\text{g}/\text{m}^3$ , respectively, and the mean  $\text{PM}_{2.5}$  concentrations  
466 are 31.2%, 40.9%, 33.0%, 28.0%, and 27.9%, respectively. The average MAEs for the United States,  
467 Canada, Europe, China, and India are 1.42  $\mu\text{g}/\text{m}^3$ , 1.36  $\mu\text{g}/\text{m}^3$ , 2.45  $\mu\text{g}/\text{m}^3$ , 6.48  $\mu\text{g}/\text{m}^3$ , and 9.56  
468  $\mu\text{g}/\text{m}^3$ , respectively; these values correspond to 15.9%, 19.4%, 17.5%, 15.6%, and 14.2%,  
469 respectively, of the mean  $\text{PM}_{2.5}$  concentration. The average correlation coefficients for the United  
470 States, Canada, Europe, China, and India are 0.88, 0.88, 0.89, 0.92, and 0.92, respectively.

471 The values of RMSE and MAE are the largest in India. The RMSE is the smallest in the United  
472 States, and the MAE is the smallest in Canada. The ratios of the RMSE and MAE to the mean are  
473 larger in Canada and Europe than in other regions and smaller in China and India than in other  
474 regions. Although the  $\text{PM}_{2.5}$  concentration varies among regions, the MAE-to-mean concentration  
475 ratio remains at approximately 16%. This finding demonstrates the stability and reliability of the  
476 model.

477 **Table 1** The results of the model's performance metrics for all sites and sites in the United States  
478 (the US), Canada, Europe, China and India.

<i>Model</i>	<i>RMSE</i> ( $\mu\text{g}/\text{m}^3$ )	<i>MAE</i> ( $\mu\text{g}/\text{m}^3$ )	$\rho$ ( <i>Pearson's</i> <i>correlation</i> )	<i>Mean</i> ( $\mu\text{g}/\text{m}^3$ )	<i>RMSE/Mean</i> (%)	<i>MAE/Mean</i> (%)
<i>All</i>	7.42	4.01	0.90	25.4	29.2	15.8
<i>the US</i>	2.78	1.42	0.88	8.9	31.2	15.9
<i>Canada</i>	2.86	1.36	0.88	7.0	40.9	19.4
<i>Europe</i>	4.63	2.45	0.89	14.0	33.0	17.5
<i>China</i>	11.62	6.48	0.92	41.5	28.0	15.6
<i>India</i>	18.73	9.56	0.92	67.0	27.9	14.2



479

480 **Figure 4** Spatial distribution (a-c) of the root mean squared error (RMSE), mean absolute error  
481 (MAE), and correlation coefficient ( $\rho$ ) between the model's estimated values and response values.  
482 Number of sites (bar) and cumulative frequency (curve) (d-e) of the RMSE, MAE, and  $\rho$ .

### 483 3.2.3 Dependence on the Distance between the PM<sub>2.5</sub> Site and the Visibility Station

484 Although the previous analysis elucidates the stability and predictive capability of the model, it is  
485 necessary to understand the potential impact of the distance between PM<sub>2.5</sub> monitoring sites and  
486 visibility stations on the model. Most PM<sub>2.5</sub> monitoring sites are in urban areas, resulting in a  
487 relatively concentrated spatial distribution. Visibility stations are strategically placed to capture the  
488 characteristics of meteorological factors and have relatively uniform spatial distributions.  
489 Consequently, visibility stations and PM<sub>2.5</sub> monitoring sites are often not collocated, resulting in a  
490 certain spatial distance between them. Therefore, we consider the impact of the distance between  
491 sites on the model's performance.

492 Figure 5 shows the relationship between the model performance ( $\rho$  and RMSE) and the distance  
493 between the visibility stations and the PM<sub>2.5</sub> monitoring sites. The average distance between all sites  
494 is 0.964°, and the correlation coefficient between the model's RMSE and distance is 0.44, which is  
495 a moderate correlation. The average  $\rho$  of 3786 sites (within a distance of 3°) is 0.90, and the average  
496 RMSE is 7.13  $\mu\text{g}/\text{m}^3$ . The RMSE values of 471 sites are greater than twice the average RMSE of  
497 all sites; however, their average  $\rho$  (0.91) is greater than the average of all sites. This finding indicates  
498 that the model's performance decreases as the distance increases.

499 For the United States, the average distance is 0.29°. The distance between the 919 (82.8%) sites was  
500 less than 0.5°, with  $\rho$  and RMSE values of 0.88 and 2.7  $\mu\text{g}/\text{m}^3$ , respectively. The  $\rho$  and RMSE of  
501 the 191 sites (more than 0.5°) are 0.88 and 3.1  $\mu\text{g}/\text{m}^3$ , respectively. The performance of the model  
502 is not significantly related to distance.



503 For Canada, 212 (69.7%) sites have distances of less than  $0.5^\circ$ , with  $\rho$  and RMSE values of 0.89  
504 and  $2.6 \mu\text{g}/\text{m}^3$ , respectively. The  $\rho$  and RMSE for 92 sites (more than  $0.5^\circ$ ) are 0.87 and  $3.3 \mu\text{g}/\text{m}^3$ ,  
505 respectively. The correlation coefficient between the RMSE and the distance is 0.33, and the  
506 correlation coefficient between the  $\rho$  and the distance is -0.17. The performance of the model  
507 decreases as the distance increases.

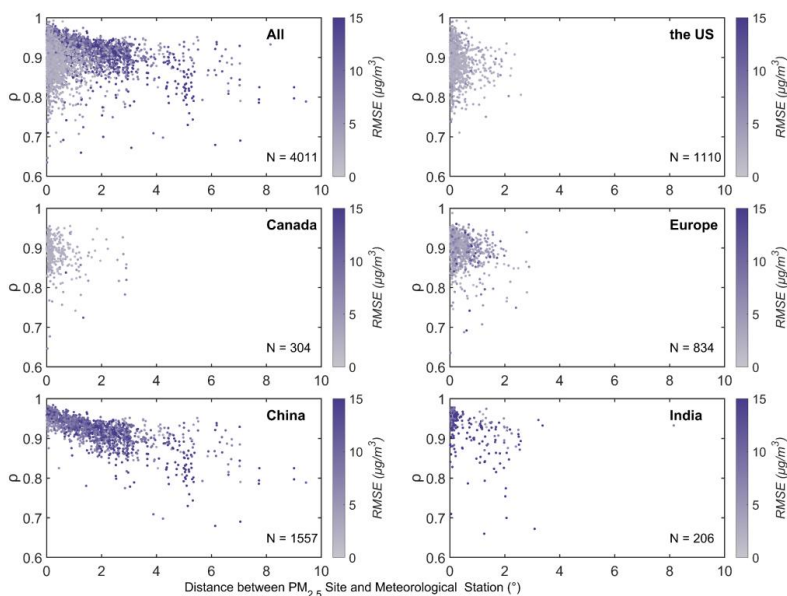
508 For Europe, 541 (64.8%) sites have distances of less than  $0.5^\circ$ , with  $\rho$  and RMSE values of 0.90 and  
509  $4.0 \mu\text{g}/\text{m}^3$ , respectively. The  $\rho$  and RMSE of the 293 sites (more than  $0.5^\circ$ ) are 0.88 and  $5.7 \mu\text{g}/\text{m}^3$ ,  
510 respectively. The correlation coefficient between the RMSE and the distance is 0.19.

511 For China, 303 (19.5%) sites have a distance of less than  $0.5^\circ$ , with  $\rho$  and RMSE values of 0.95 and  
512  $9.5 \mu\text{g}/\text{m}^3$ , respectively. The  $\rho$  and RMSE for 1254 sites (more than  $0.5^\circ$ ) are 0.91 and  $12.1 \mu\text{g}/\text{m}^3$ ,  
513 respectively. The correlation coefficient between the RMSE and the distance is 0.23. The correlation  
514 coefficient between  $\rho$  and distance is -0.71. As the distance increases, the correlation coefficient  
515 significantly decreases.

516 For India, the  $\rho$  and RMSE of 117 (56.8%) sites with a distance of less than  $0.5^\circ$  are 0.94 and  $18.7$   
517  $\mu\text{g}/\text{m}^3$ , respectively. The  $\rho$  and RMSE of 89 sites (more than  $0.5^\circ$ ) are 0.89 and  $18.8 \mu\text{g}/\text{m}^3$ ,  
518 respectively. The correlation coefficient between  $\rho$  and distance is -0.36.

519 The above results indicate no significant correlation between model performance and distance in  
520 the United States and Europe, as these regions have adequate visibility stations. However, in China,  
521 India, and Canada, the performance of models is influenced by distance. Particularly in China, due  
522 to the limited number of visibility stations, although the correlation coefficient decreases with  
523 distance, there is no significant change in the RMSE. The correlation coefficient for visibility  
524 remains near 0.4. Even when the distance between two visibility stations reaches 1000 km, the  
525 maximum correlation coefficient for visibility remains near 0.4 (Fei et al., 2023). To acquire more  
526  $\text{PM}_{2.5}$  sample data, we do not disregard these distant sites since the models still shows a good  
527 performance for these sites. Nevertheless, more sufficient visibility stations in the same locations  
528 can enhance the model's performance.





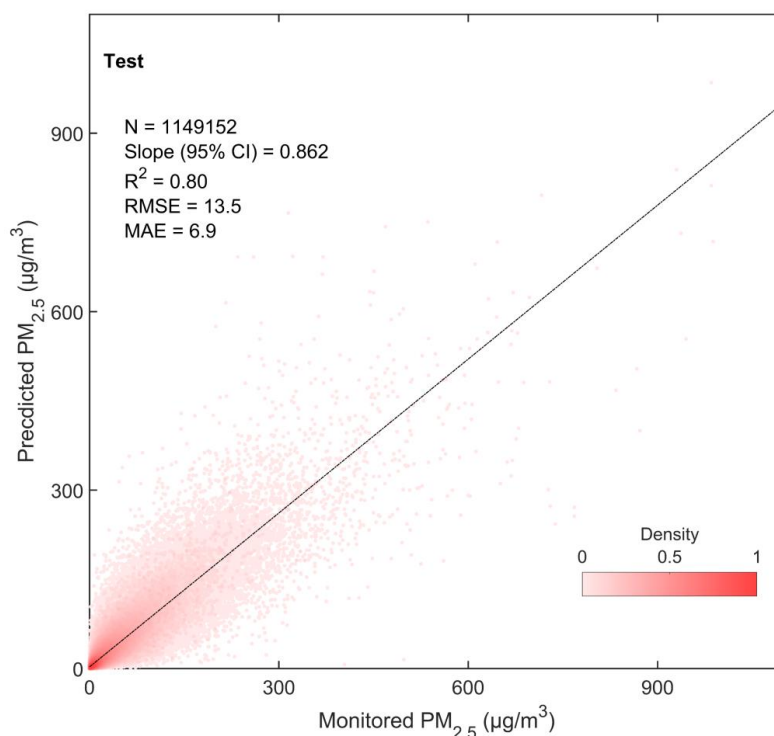
529

530 **Figure 5** Scatter plots of the distance between the PM<sub>2.5</sub> site and visibility station and the model's  
531 correlation coefficient ( $\rho$ ) for all sites and sites in the United States, Canada, Europe, China, and  
532 India. The color bar represents the root mean square error (RMSE) of the model. N is the number  
533 of sites.

### 534 3.3 Evaluation of Model's Predictive Ability

#### 535 3.3.1 For All Data

536 A total of 1,149,152 pairs of test data is employed to evaluate the model's predictive ability. Figure  
537 6 shows the density scatter plot between the predicted PM<sub>2.5</sub> concentration and the test PM<sub>2.5</sub>  
538 concentration. The results indicate that the linear regression coefficient is  $0.862 \pm 0.001$  within a  
539 95% confidence interval,  $R^2$  is 0.80, RMSE is  $13.5 \mu\text{g}/\text{m}^3$ , and MAE is  $6.9 \mu\text{g}/\text{m}^3$ . Previous studies  
540 have shown that the  $R^2$  range of the model's predictive results at the daily scale is 0.42-0.89, and the  
541 RMSE range is  $9.59\text{-}32.09 \mu\text{g}/\text{m}^3$  (Gui et al., 2020; Zhong et al., 2021). The test results exhibit  
542 excellent predictive capability.



543

544 **Figure 6** Density scatter plot (a) between the predicted  $PM_{2.5}$  concentration and monitored  $PM_{2.5}$   
545 concentration of the test results at the daily scale. The dashed black line is the linear regression line.  
546  $N$  is the length of the data pairs, and Slope is the linear regression coefficient within a 95%  
547 confidence interval (CI).  $R^2$  is the coefficient of determination, RMSE is the root mean square error,  
548 and MAE is the mean absolute error.

### 549 3.3.2 For the Site and Region Scales

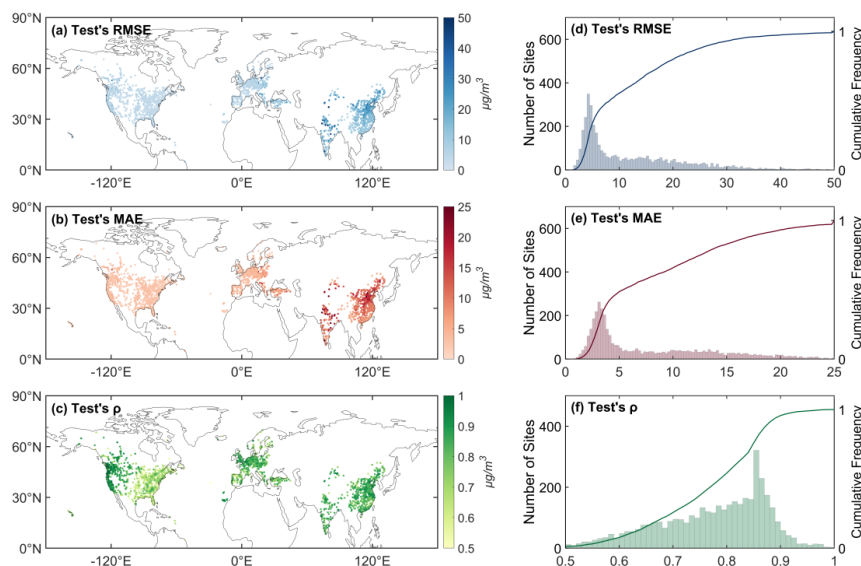
550 We analyze the test results for Canada, the United States, Europe, China, and India to assess the  
551 predictive ability of the model in different regions. Figure 7 shows the spatial distributions of the  
552 test RMSE, MAE, and  $\rho$  and their frequency and cumulative frequency distributions. Table 2 lists  
553 the test results of the metrics.

554 For all sites, the average RMSE is  $12.60 \mu\text{g}/\text{m}^3$ . The RMSE-to-mean ratio is 48.6%. The average  
555 MAE is  $8.52 \mu\text{g}/\text{m}^3$ . The MAE-to-mean ratio is 32.9%. The average  $\rho$  is 0.77.

556 For the United States, the RMSE, MAE, and  $\rho$  are  $4.90 \mu\text{g}/\text{m}^3$ ,  $3.15 \mu\text{g}/\text{m}^3$ , and 0.71, respectively.  
557 For Canada, the RMSE, MAE, and  $\rho$  are  $4.89 \mu\text{g}/\text{m}^3$ ,  $3.01 \mu\text{g}/\text{m}^3$ , and 0.74, respectively. The results  
558 in the United States and Canada are better in the west than in the east. The RMSE, MAE, and  $\rho$  for  
559 Europe are  $7.54 \mu\text{g}/\text{m}^3$ ,  $4.91 \mu\text{g}/\text{m}^3$ , and 0.77, respectively. For China, the RMSE, MAE, and  $\rho$  are  
560  $20.16 \mu\text{g}/\text{m}^3$ ,  $13.81 \mu\text{g}/\text{m}^3$ , and 0.81, respectively. For India, the RMSE, MAE, and  $\rho$  are  
561  $28.84 \mu\text{g}/\text{m}^3$ ,  $19.57 \mu\text{g}/\text{m}^3$ , and 0.83, respectively. The results show that in developing regions (China and



562 India),  $\rho$  is better than that in developed regions (the United States, Canada, and Europe), which  
 563 means that the predictive ability of the model is better for severely polluted regions.



564

565 **Figure 7** Spatial distribution (a-c) of the root mean squared error (RMSE), mean absolute error  
 566 (MAE), and correlation coefficient ( $\rho$ ) between the model's predicted values and test values.  
 567 Number of sites (bar) and cumulative frequency (curve) (d-e) of the RMSE, MAE, and  $\rho$ .

568 **Table 2** The test results of the model's performance metrics for all sites and sites in the United States,  
 569 Canada, Europe, China and India.

<i>Test</i>	<i>RMSE</i> ( $\mu\text{g}/\text{m}^3$ )	<i>MAE</i> ( $\mu\text{g}/\text{m}^3$ )	$\rho$ (Pearson's correlation)	<i>Mean</i> ( $\mu\text{g}/\text{m}^3$ )	<i>RMSE/Mean</i> (%)	<i>MAE/Mean</i> (%)
<i>All</i>	12.60	8.52	0.77	25.9	48.6	32.9
<i>America</i>	4.90	3.15	0.71	9.1	53.8	34.6
<i>Canada</i>	4.89	3.01	0.74	7.2	67.9	41.1
<i>Europe</i>	7.54	4.91	0.77	14.4	52.3	34.1
<i>China</i>	20.16	13.81	0.81	42.2	47.7	32.7
<i>India</i>	28.94	19.62	0.83	67.6	42.8	29.0

570 **3.4 Uncertainties and Limitations**

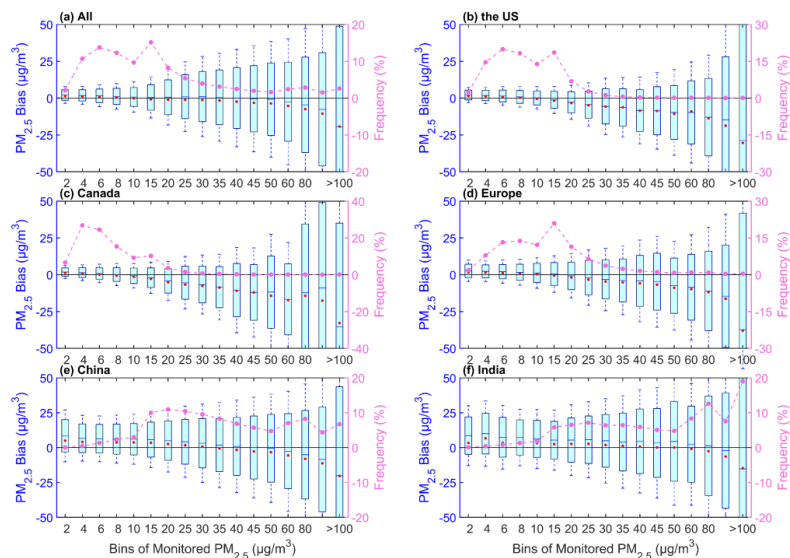
571 **3.4.1 Uncertainty in the Pollution Level**

572 Figure 8 shows the uncertainty in the predicted  $\text{PM}_{2.5}$  concentration with respect to the pollution  
 573 level of the monitored  $\text{PM}_{2.5}$ . For all sites, the uncertainty in the bias increases as the pollution  
 574 increases. The mean bias and the median bias shift from positive to negative with increasing  
 575 pollution levels. The mean bias of 88.4% of the data is less than  $2 \mu\text{g}/\text{m}^3$ . A mean bias of 86.9%



576 ( $<40 \mu\text{g}/\text{m}^3$ ) is positive, and a median bias of 38.9% ( $<8 \mu\text{g}/\text{m}^3$ ) is positive. This result indicates that  
577 the model overestimates at low concentrations.

578 The bias for each region also increases with pollution level. For sites in the United States, the mean  
579 bias of 92.1% is less than  $2 \mu\text{g}/\text{m}^3$ . A total of 69.1% ( $<10 \mu\text{g}/\text{m}^3$ ) are positive. For sites in Canada,  
580 the mean bias of 82.5% is less than  $2 \mu\text{g}/\text{m}^3$ . A total of 73.3% are positive ( $<8 \mu\text{g}/\text{m}^3$ ). Among the  
581 data ( $<8 \mu\text{g}/\text{m}^3$ ), 57.9% of the median is positive. For sites in Europe, the mean bias of 64.8% is less  
582 than  $2 \mu\text{g}/\text{m}^3$ , and 69.8% is positive. A total of 49.0% of the median is positive. For sites in China,  
583 81.8% of the bias is less than  $5 \mu\text{g}/\text{m}^3$  and 68.9% ( $<45 \mu\text{g}/\text{m}^3$ ) is positive. A total of 48.0% ( $<30$   
584  $\mu\text{g}/\text{m}^3$ ) of the median is positive. For sites in India, 80.5% of the bias is less than  $8 \mu\text{g}/\text{m}^3$ , and 73.5%  
585 ( $<80 \mu\text{g}/\text{m}^3$ ) is positive. A total of 52.6% ( $<60 \mu\text{g}/\text{m}^3$ ) of the median values are positive.



586

587 **Figure 8** Boxplots of the pollution level and bias (predicted  $\text{PM}_{2.5}$  - monitored  $\text{PM}_{2.5}$ ) for all sites  
588 (a), sites in the United States (b), Canada (c), Europe (d), China (e), and India (f). The box's upper  
589 and lower limits represent  $\pm 1$  standard deviation, the whiskers represent 2 times the standard  
590 deviation, the red circle represents the median, and the short line represents the mean bias. The  
591 frequency (%) on the right y-axis represents the percentage of data with different pollution levels  
592 (dashed line).

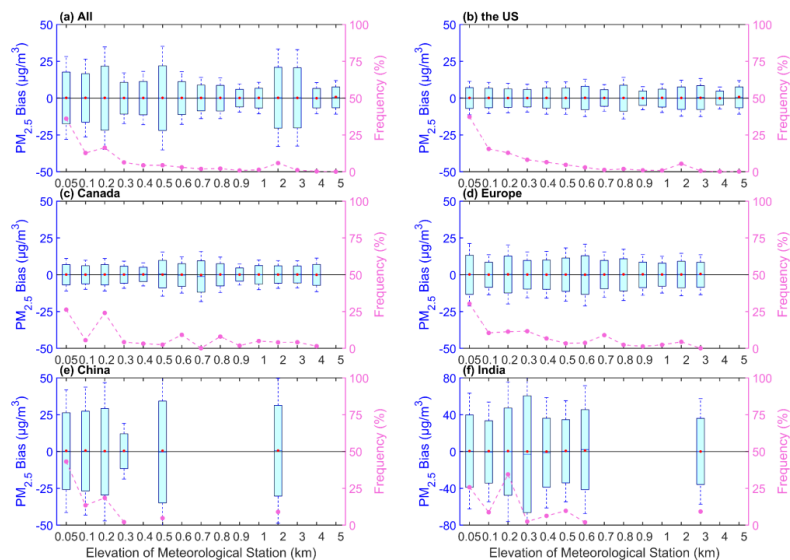
### 593 3.4.2 Uncertainty in the Station Elevation

594 With the spatial variability in  $\text{PM}_{2.5}$ , we analyze the mean bias at different station elevations. Figure  
595 9 shows the relationships between the elevations of the visibility stations and the bias. The bias  
596 exhibits variations across different elevations for all sites. A total of 89.5% of the data are at an  
597 elevation of 1 km. The mean bias ranges from  $-0.1$  to  $0.5 \mu\text{g}/\text{m}^3$ . High uncertainties in bias occur at  
598 elevations below 0.2 km, 0.4-0.5 km, and 1-3 km. A total of 88.5% of the data have positive mean  
599 biases. Negative biases are observed at elevations of 0.6-0.8 km, 3 km, and 5 km. A total of 57.7%  
600 of the data have a positive median. This finding indicates a nonsignificant overestimation of the



601 predicted  $PM_{2.5}$  concentration due to the various elevations.

602 The bias patterns vary across regions. For the United States, 92.8% of the data correspond to  
603 elevations below 1 km. The mean bias ranges from -0.1 to  $0.5 \mu\text{g}/\text{m}^3$ . A total of 88.8% of the mean  
604 biases are positive, and the median of 99% is positive. For Canada, 90.1% of the data correspond to  
605 elevations below 1 km. The mean bias ranges from -0.1 to 0.2. A total of 46.5% of the mean bias is  
606 positive, and the median is positive except at elevations of 0.7 km and 4 km. A higher uncertainty  
607 in the bias occurs at elevations ranging from 0.5-0.8 km. For Europe, 92.9% of the data correspond  
608 to elevations below 1 km. The bias ranges from -0.2 to  $0.2 \mu\text{g}/\text{m}^3$ . A total of 62.7% of the mean bias  
609 is negative, and the median is positive. High standard deviations are observed at elevations of 0.2  
610 km, 0.05 km, and 0.5-0.6 km. A significant bias occurs at 0.6 km. For China, 81.9% of the data  
611 correspond to elevations below 0.5 km. The median is positive, and the mean bias is positive except  
612 at 0.1 km. The lowest standard deviation occurs at an elevation of 0.3 km. For India, the mean bias  
613 ranges from -0.3 to  $0.9 \mu\text{g}/\text{m}^3$ . The highest bias occurs at an elevation of 0.3 km. There is a negative  
614 mean bias in the range of 0.1-0.4 km. The medians are positive except at an elevation of 0.4 km.



615

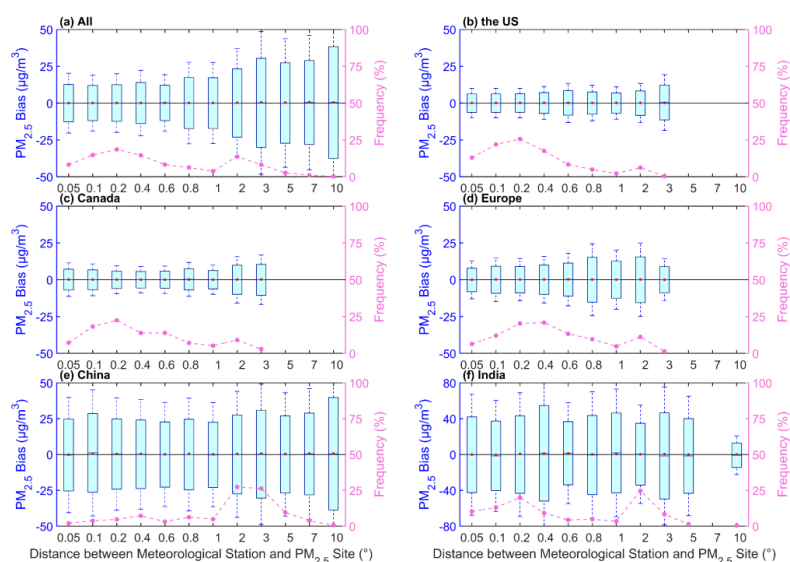
616 **Figure 9** Boxplots of the elevation of the visibility station and bias (predicted  $PM_{2.5}$  - monitored  
617  $PM_{2.5}$ ) for all sites (a), sites in the United States (b), Canada (c), Europe (d), China (e), and India (f).  
618 The box's upper and lower limits represent  $\pm 1$  standard deviation, the whiskers represent 2 times the  
619 standard deviation, the red circle represents the median, and the short line represents the mean bias.  
620 The frequency (%) on the right y-axis represents the percentage of data at different pollution levels  
621 (dashed line).

### 622 3.4.3 Uncertainty in the Station Distance

623 As the visibility stations and  $PM_{2.5}$  sites are not collocated, we analyze the  $PM_{2.5}$  mean bias at  
624 different distances. Figure 10 shows the distance between the visibility of the station and the  $PM_{2.5}$   
625 site and bias. For all sites, the standard deviation gradually increases with distance, indicating an



626 increase in uncertainty with increasing distance. Except at distances of 0.05° and 1°, the mean bias  
627 is positive. The median is positive. For each region, the distance of the largest average bias is 3° in  
628 the United States, 3° in Canada, 0.8° in Europe, 10° in China, and 0.4° in India. The distances are  
629 below 1° in the United States, Canada, Europe, and India, while they are 1-3° in China. This finding  
630 is due to the limited number of visibility sites in China. The mean bias exhibits greater uncertainties  
631 in China and India.



632

633 **Figure 10** Boxplots of the distance between the visibility station and the PM<sub>2.5</sub> site and bias  
634 (predicted PM<sub>2.5</sub> - monitored PM<sub>2.5</sub>) for all sites (a), sites in the United States (b), Canada (c), Europe  
635 (d), China (e), and India (f). The box's upper and lower limits represent ±1 standard deviation, the  
636 whiskers represent 2 times the standard deviation, the red circle represents the median, and the short  
637 line represents the mean bias. The frequency (%) on the right y-axis represents the percentage of  
638 data under different pollution levels (dashed line).

#### 639 3.4.4 Discussion on the Uncertainties and Limitations

640 There are some uncertainties and limitations in this study. The upper limit of visibility (PM<sub>2.5</sub>) is 10  
641 km (1000 µg/m<sup>3</sup>), which can cause some uncertainties in modeling. The maximum distance for  
642 spatial matching between the visibility stations and PM<sub>2.5</sub> monitoring sites is 10° due to the spatial  
643 variability in aerosols, which may increase the uncertainty in the estimated PM<sub>2.5</sub> concentration. The  
644 boundary layer height is closely related to the vertical structure of PM<sub>2.5</sub>, and reanalysis data may  
645 introduce uncertainty to the model. Because of the nonuniform vertical distribution of aerosols, the  
646 different elevations of the visibility stations and the PM<sub>2.5</sub> monitoring sites further increase the  
647 uncertainty in estimating PM<sub>2.5</sub>. In addition, the spatial coverage of visibility stations, especially in  
648 China, is limited, which may increase the uncertainty in the representativeness of regional PM<sub>2.5</sub>  
649 trends and pollution levels. With the increasing human concern about air pollution and the  
650 implementation of pollution control measures, the types of major atmospheric pollutants have



651 changed, the composition of particulate matter has also evolved, the scattering and absorption  
652 characteristics may have changed, and the relationship between visibility and PM<sub>2.5</sub> may change.  
653 These changes may lead to uncertainty in estimating historical PM<sub>2.5</sub>, especially before 2000  
654 (ground and satellite observations are limited). Despite these limitations, we establish a long-term  
655 PM<sub>2.5</sub> dataset based on visibility from 1959 to 2022, providing insights into the long-term  
656 spatiotemporal characteristics of PM<sub>2.5</sub> in the Northern Hemisphere.

#### 657 **4 Comparisons with Other PM<sub>2.5</sub> Datasets**

658 We compare the monthly estimated PM<sub>2.5</sub> with the PM<sub>2.5</sub> of those derived from a satellite AOD and  
659 two reanalysis datasets, including (1) ACAG, the monthly satellite-derived PM<sub>2.5</sub> from 1998 to 2022  
660 (Van Donkelaar et al., 2019; Hammer et al., 2020); (2) MERRA-2, the monthly PM<sub>2.5</sub> from 1980 to  
661 2022 (Buchard et al., 2016; Buchard et al., 2017; Gelaro et al., 2017); and (3) CAMS, the monthly  
662 PM<sub>2.5</sub> from 2003 to 2022 (Inness et al., 2019). The time ranges for comparing the estimated PM<sub>2.5</sub>  
663 with the ACAG, MERRA-2, and CAMS data are 1998-2022, 1980-2022, and 2003-2022,  
664 respectively. The monthly average should meet a minimum requirement of at least ten days per  
665 month.

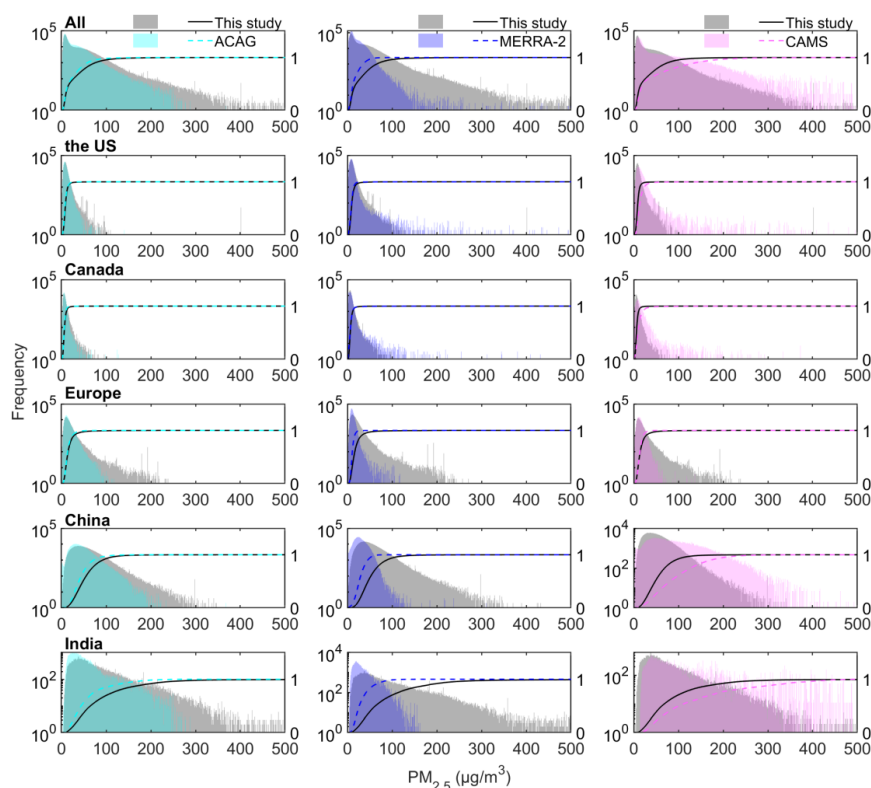
#### 666 **4.1 Monthly Frequency and Annual Cycle of PM<sub>2.5</sub>**

667 We compare the frequency of the estimated PM<sub>2.5</sub> concentration at different pollution levels, with  
668 an interval of 1 µg/m<sup>3</sup>, with three other datasets. Figure 11 shows the monthly PM<sub>2.5</sub> frequencies of  
669 the estimated, ACAG, MERRA-2, and CAMS datasets for all sites and regional sites.

670 Compared with the ACAG data, they exhibit similar frequency distributions. However, the  
671 frequency of estimated PM<sub>2.5</sub> concentrations is greater at high pollution levels at all sites. Regionally,  
672 the frequency distributions are similar at different pollution levels in the United States and Canada.  
673 In Europe, China, and India, the frequency of high concentrations is greater than that of the ACAG.

674 Compared with the MERRA-2 data, the frequency distribution of the estimated data is similar to  
675 that of the ACAG for all the sites. Regionally, the frequency distributions of the estimates are  
676 comparable in the United States and Canada. However, in Europe, China, and India, the differences  
677 in the frequency of high pollution levels are greater than those in the ACAG.

678 Compared with the CAMS data, the frequency distributions at high pollution levels are similar, but  
679 the frequency at high pollution levels is lower. Regionally, Europe differs from other regions, as the  
680 frequency of high pollution levels is higher.



681

682 **Figure 11** Frequency (left axis) and cumulative frequency (right axis) of monthly  $PM_{2.5}$ . The time  
 683 range of the estimated  $PM_{2.5}$  corresponds to the time range of the three datasets (ACAG from 1998  
 684 to 2022, MERRA-2 from 1980 to 2022, and CAMS from 2003 to 2022). The bins range from 0 to  
 685 500  $\mu g/m^3$  with an interval of 1  $\mu g/m^3$ .

686 In Figure 12, we compare the multiyear monthly average  $PM_{2.5}$  concentration with that of the three  
 687 datasets. For all sites, the correlation coefficients between the estimated and ACAG, MERRA-2,  
 688 and CAMS data are 0.99, 0.42, and 0.93, respectively, and the average biases (average relative biases)  
 689 are 6.6  $\mu g/m^3$  (26%), 14.1  $\mu g/m^3$  (76%), and -19.1  $\mu g/m^3$  (-37%), respectively. The estimated  
 690 multiyear average monthly  $PM_{2.5}$  concentrations are higher for ACAG and MERRA-2 and lower  
 691 for CAMS. The correlation coefficient is highest for ACAG and lowest for MERRA-2.

692 Compared with the ACAG data, the correlation coefficients are 0.97, 0.96, 0.98, 0.99, and 0.99, with  
 693 average biases (average relative biases) of 0.8  $\mu g/m^3$  (9%), 0.5  $\mu g/m^3$  (7%), 2.2  $\mu g/m^3$  (16%), 10.8  
 694  $\mu g/m^3$  (26%), and 31.4  $\mu g/m^3$  (62%) in the United States, Canada, Europe, China, and India,  
 695 respectively. The annual variations in the two datasets are nearly consistent across all regions. The  
 696 bias is less than 10% for the United States and Canada, while India exhibits the largest bias.

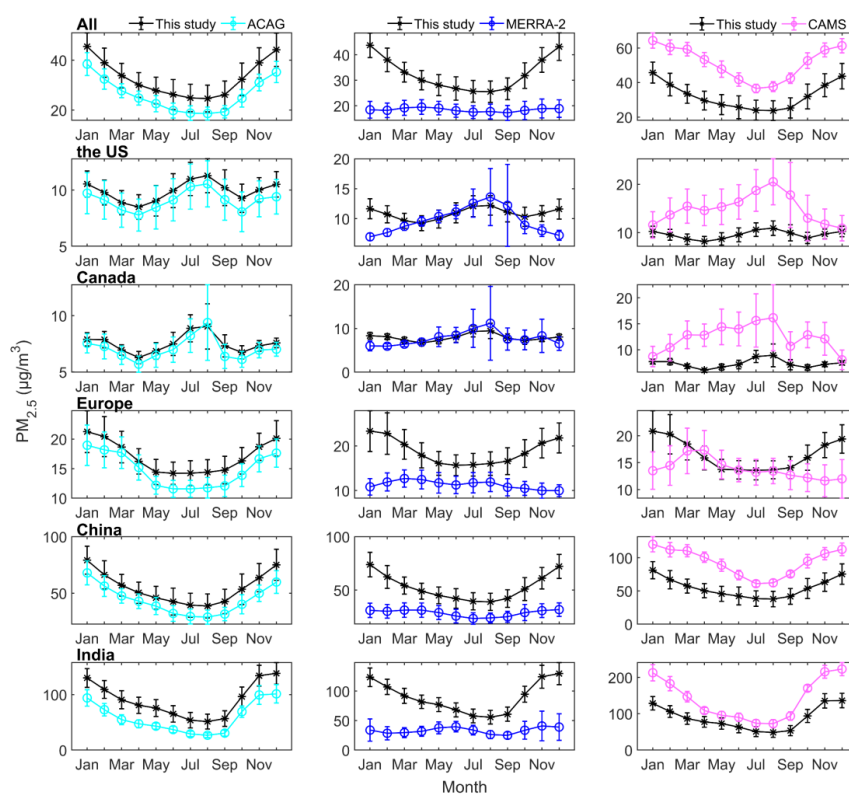
697 Compared with the MERRA-2 data, the correlation coefficients are 0.30, 0.61, -0.25, 0.80, and 0.45,  
 698 with average biases (average relative biases) of 1.1  $\mu g/m^3$  (16%), 0.2  $\mu g/m^3$  (5%), 7.5  $\mu g/m^3$  (67%),  
 699 24.1  $\mu g/m^3$  (83%), and 56.1  $\mu g/m^3$  (169%) in the United States, Canada, Europe, China, and India,





700 respectively. There are differences in the annual variations between the two datasets, particularly  
 701 during winter (November to January) and spring (February to March), in all regions. The largest  
 702 difference occurs in March and September to December in Europe, showing the opposite trend. The  
 703 highest correlation coefficient is observed in China, which has the second largest bias. The largest  
 704 bias is in India.

705 Compared with the CAMS data, the correlation coefficients are 0.29, 0.22, 0.02, 0.91, and 0.98,  
 706 with average biases (average relative biases) of  $-5.4 \mu\text{g}/\text{m}^3$  (-34%),  $-5.0 \mu\text{g}/\text{m}^3$  (-38%),  $2.7 \mu\text{g}/\text{m}^3$   
 707 (21%),  $-38.7 \mu\text{g}/\text{m}^3$  (-42%), and  $-52.7 \mu\text{g}/\text{m}^3$  (-36%) in the United States, Canada, Europe, China,  
 708 and India, respectively. The annual variations between the CAMS and ACAG data are similar in  
 709 China and India but have more significant biases. The smallest differences in the United States and  
 710 Canada occur in January and December. In Europe, the months with more significant biases are  
 711 January to March and September to December, while biases are smaller in other months.



712  
 713 **Figure 12** Multiyear monthly average  $\text{PM}_{2.5}$  of our data and the three datasets. The time range of  
 714 the estimated  $\text{PM}_{2.5}$  corresponds to the time range of the three datasets (ACAG data from 1998 to  
 715 2022, MERRA-2 data from 1980 to 2022, and CAMS data from 2003 to 2022).

#### 716 4.2 Time Series at the Annual Scale

717 Figure 13 shows the annual average  $\text{PM}_{2.5}$  concentration from 1959 to 2022 in different regions,  
 718 along with a comparison to the  $\text{PM}_{2.5}$  concentrations derived from other datasets. Another dataset is



719 used for comparison in China: the monthly  $PM_{2.5}$  of the CHAP from 2000 to 2021 (Wei et al., 2020b;  
720 Wei et al., 2021). We use correlation coefficients, mean bias and mean relative bias to compare the  
721 relationships and differences among the  $PM_{2.5}$  datasets.

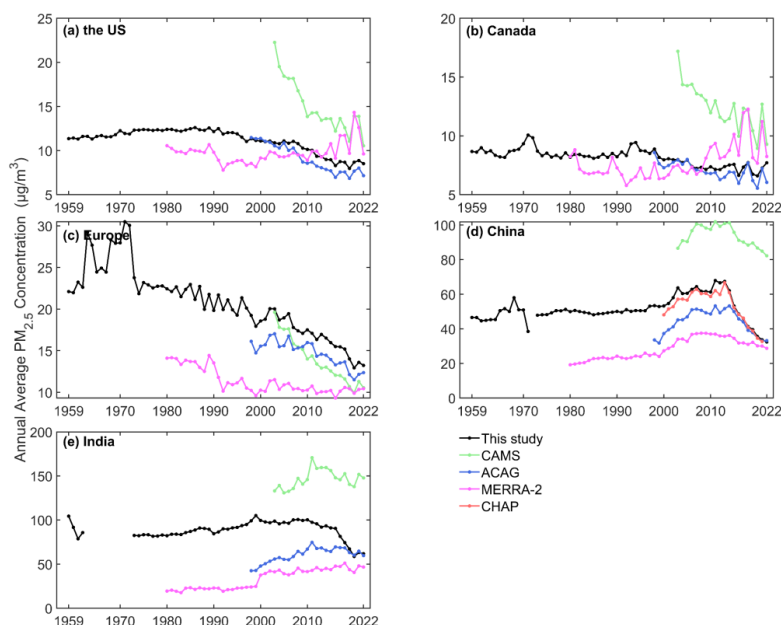
722 In the United States, the estimated  $PM_{2.5}$  concentrations exhibit correlation coefficients of 0.96, 0.88,  
723 and -0.38 with the ACAG, CAMS, and MERRA-2 data, respectively; the mean bias (mean relative  
724 bias) is 0.8 (10%), -5.4 (-35%), and 1.1 (13%) for each dataset, respectively.

725 In Canada, the estimated  $PM_{2.5}$  concentrations exhibit correlation coefficients of 0.84, 0.62, and -  
726 0.46 with the ACAG, CAMS, and MERRA-2 data, respectively; the mean bias (mean relative bias)  
727 is  $0.5 \mu\text{g}/\text{m}^3$  (7%),  $-5.1 \mu\text{g}/\text{m}^3$  (-40%), and  $0.2 \mu\text{g}/\text{m}^3$  (6%) for each dataset, respectively.

728 In Europe, the estimated  $PM_{2.5}$  concentrations exhibit correlation coefficients of 0.96, 0.96, and 0.76  
729 with the ACAG, CAMS, and MERRA-2 data, respectively; the mean bias (mean relative bias) is  $2.3$   
730  $\mu\text{g}/\text{m}^3$  (15%),  $2.6 \mu\text{g}/\text{m}^3$  (20%), and  $7.5 \mu\text{g}/\text{m}^3$  (66%) for each dataset, respectively.

731 In China, the estimated  $PM_{2.5}$  concentrations exhibit correlation coefficients of 0.78, 0.98, 0.81, and  
732 0.51 with the ACAG, CHAP, CAMS, and MERRA-2 data, respectively; the mean bias (mean  
733 relative bias) is  $10.7 \mu\text{g}/\text{m}^3$  (24%),  $2.5 \mu\text{g}/\text{m}^3$  (4%),  $-39.1 \mu\text{g}/\text{m}^3$  (-42%), and  $24 \mu\text{g}/\text{m}^3$  (90%) for  
734 each dataset, respectively.

735 In India, the estimated  $PM_{2.5}$  concentrations exhibit correlation coefficients of -0.3, -0.02, and -0.09  
736 with the ACAG, CAMS, and MERRA-2 data, respectively; the mean bias (mean relative bias) is  
737  $29.9 \mu\text{g}/\text{m}^3$  (53%),  $-58.9 \mu\text{g}/\text{m}^3$  (-40%), and  $56.1 \mu\text{g}/\text{m}^3$  (203%) for each dataset, respectively. From  
738 2013 to 2022, the correlation coefficients with the ACAG and CAMS data are 0.71 and 0.70,  
739 respectively. The trend of visibility declines from 1961 to 2008. The frequency of visibility  
740 (exceeding 10 km) in the afternoon decreases by 46%, and the frequency of visibility (below 4 km)  
741 in the morning increases by 21% (Jaswal et al., 2013), particularly in the central and northern regions.  
742 The low cloud cover significantly increases from 1960 to 2010 in the Indo-Gangetic Plain and the  
743 northwestern and eastern coasts of India (Jaswal et al., 2017). The average total cloud cover is 3.4  
744 okta from 1960 to 2007, with a decrease of 0.07 okta/decade (Jaswal, 2010). However, the indirect  
745 impact of aerosols on cloud formation do not influence cloud cover (Ramanathan et al., 2005). The  
746 prevalence of clouds poses challenges for satellite retrievals in these areas, potentially contributing  
747 to substantial disparities between  $PM_{2.5}$  concentrations estimated based on visibility and satellite  
748 retrievals. The CAMS reanalysis data are calibrated using satellite data and thus show consistency  
749 with the trend in AOD retrievals from satellites; the anthropogenic emission data are from the  
750 MACCity inventory (Inness et al., 2019), and there are significant variations among different  
751 anthropogenic emission inventories, particularly before 2010, which leads to substantial  
752 uncertainties in India (Granier et al., 2011; Liu et al., 2022). These issues exist to a greater or lesser  
753 extent in other regions, which may contribute to the increased disparities between estimated  $PM_{2.5}$   
754 and reanalysis data before 2012.



755

756 **Figure 13** Annual mean  $PM_{2.5}$  concentration from 1959 to 2022 in the United States (US) (a),  
757 Canada (b), Europe (c), China (d), and India (e). The other four datasets are ACAG from 1998 to  
758 2022, CHAP from 2000 to 2021, MERRA-2 from 1980 to 2022, and CAMS from 2003 to 2022.

### 759 4.3 Discussion on the Differences among the $PM_{2.5}$ Datasets

760  $PM_{2.5}$  is considered a pollutant that decreases visibility. There is a negative correlation between  
761 visibility and  $PM_{2.5}$  concentration, and the reciprocal of visibility is proportional to the extinction  
762 coefficient, which is closely related to the concentration of particulate matter (Wang et al., 2012;  
763 Zhang et al., 2017; Zhang et al., 2020). Prior to the widespread implementation of  $PM_{2.5}$   
764 measurements or lack of measurement of particulate matter, visibility is often used as a proxy for  
765 particulate matter pollution (Huang et al., 2009; Singh et al., 2020). It is the basis for using visibility  
766 to estimate  $PM_{2.5}$  concentration. Studies have shown that meteorological observations such as  
767 temperature and humidity also play an important role in estimating  $PM_{2.5}$  concentration using  
768 visibility (Shen et al., 2016; Xue et al., 2019; Zhong et al., 2021). The advantages of ground-based  
769 visibility and other meteorological variables observations include long-term records, high temporal  
770 resolution, and good data completeness, and the visibility observations from airports can be traced  
771 back to 1959 in this study. Therefore, we employ a machine learning approach to establish the  
772 relationship between  $PM_{2.5}$  and visibility and other meteorological variables, and estimate the long-  
773 term historical  $PM_{2.5}$  concentration from 1959 to 2022, and discuss the limitations and uncertainties.  
774 It should be noted that not all sites of  $PM_{2.5}$  have the time range from 1959 to 2022, which depends  
775 on the record length of matched visibility station.

776 There are differences between  $PM_{2.5}$  based on visibility,  $PM_{2.5}$  based on satellite retrievals, and



777  $PM_{2.5}$  of reanalysis.  $PM_{2.5}$  based on satellite retrievals typically requires consideration of aerosol  
778 vertical profiles usually provided by observations, assumptions, or chemical transport models to  
779 obtain the aerosol properties near the surface (Van Donkelaar et al., 2010; Wei et al., 2019b; Van  
780 Donkelaar et al., 2021).  $PM_{2.5}$  from reanalysis usually requires accurate meteorological fields and  
781 emission inventories. Although ERA5 has provided meteorological reanalysis since 1940, the  
782 historical emission inventories and physical-chemical mechanisms in the chemical transport model  
783 still have significant uncertainties, which increase the uncertainty in particulate matter concentration.  
784 Additionally, the assimilated data in reanalysis mainly consist of satellite AOD and ground-based  
785 AOD, aiming to improve column aerosol properties, without considering near-surface  $PM_{2.5}$   
786 (Buchard et al., 2017; Gelaro et al., 2017; Provençal et al., 2017; Huijnen et al., 2019; Inness et al.,  
787 2019; Ali et al., 2022). These factors contribute to the differences in estimating  $PM_{2.5}$  concentration  
788 among the three methods.

789 In this study, the upper limit of the estimated daily  $PM_{2.5}$  concentration is set to  $1000 \mu\text{g}/\text{m}^3$  because  
790 the  $PM_{2.5}$  concentration is greater than 500 during heavy pollution weather, which may contribute  
791 to the higher frequency at high pollution levels than in the other datasets. We do not delete visibility  
792 records during sand and dust weather when preprocessing the data, which may lead to an  
793 overestimation of  $PM_{2.5}$  in dusty areas, such as northern China and northwestern India.

794 The frequency and monthly/annual variations in our data are consistent with those of  $PM_{2.5}$  based  
795 on satellite retrievals (ACAG and CHAP). The concentration level is higher than in those datasets  
796 because their upper limits are lower. The AOD is a physical quantity that describes the properties of  
797 aerosol columns. It is important to consider the vertical structure of aerosols when establishing a  
798 connection between AOD and near-ground  $PM_{2.5}$ . Van Donkelaar et al. (2006; 2010) demonstrated  
799 that aerosol vertical profile errors in chemical transport models and AOD retrieval and sampling  
800 result in an approximately 25% uncertainty of one standard deviation. Sensitivity testing shows that  
801 a 1% estimation error in the AOD can lead to a 0.27% estimation error in the  $PM_{2.5}$  concentration  
802 (Wei et al., 2021). Visibility is a near-surface observation that is not affected by clouds or surface  
803 types and has high temporal resolution (Liu et al., 2017; Singh et al., 2020; Zhong et al., 2021). In  
804 section 3.4, the uncertainty analysis provides an explanation for the overestimation.

805 In section 2.6.3, we introduce the chemical model, emission, and assimilation of MERRA-2. The  
806  $PM_{2.5}$  concentration from MERRA-2 does not include nitrates, and the assimilation of AOD mainly  
807 provides constraints on aerosols after 2000 (Buchard et al., 2016; Randles et al., 2017; Ali et al.,  
808 2022). The lack of nitrate is a limitation in areas with high nitrate concentrations. For example, an  
809 extreme pollution event over China in January 2013 is not captured well (Buchard et al., 2017). Ali  
810 et al. (2022) used  $1.4 \times [\text{SO}_4^{2-}]$  to represent nitrate concentration, and the results showed a  
811 correlation coefficient of 0.55 with the observed  $PM_{2.5}$ . Compared to the ACAG over the United  
812 States, which has a low nitrate concentration, the MERRA-2 surface  $PM_{2.5}$  concentration is greater  
813 in rural areas than in urban and suburban areas, with high and localized emissions reducing the  
814 representation of the grid mean  $PM_{2.5}$  (Buchard et al., 2017). Therefore, the lack of nitrate and  
815 insufficient assimilation data are the key factors leading to the significant differences between the  
816 two datasets.

817 In section 2.6.4, we introduce the CAMS  $PM_{2.5}$ . The  $PM_{2.5}$  concentration from CAMS is  
818 significantly greater than the estimated  $PM_{2.5}$  concentration and follows a similar annual cycle,



819 except in Europe. In Europe, the CO and NO<sub>2</sub> concentrations in CAMS are lower than those in  
820 winter (Flemming et al., 2015), which may lead to the underestimation of nitrate emissions and its  
821 precursors, resulting in the underestimation of PM<sub>2.5</sub> concentrations. Some studies have reported  
822 similar results (Kong et al., 2021; Ryu and Min, 2021; Ali et al., 2022; Jin et al., 2022). This finding  
823 may be related to the vertical section structure, composition, and microphysical properties of  
824 aerosols (Ali et al., 2022). Because NO<sub>2</sub> emissions are obtained by multiplying CO emissions by a  
825 factor of 0.2, the uncertainty in nitrate increases. Studies have shown that the uncertainties in  
826 MACCity (Huijnen et al., 2019) and dust (Ukhov et al., 2020) also cause overestimation in CAMS  
827 PM<sub>2.5</sub>.

828 Overall, our PM<sub>2.5</sub> dataset has good consistency with PM<sub>2.5</sub> based on satellite AOD data. There are  
829 some differences in the reanalysis PM<sub>2.5</sub> concentrations. We also hope that our dataset can provide  
830 auxiliary support for reanalysis datasets.

## 831 **5 PM<sub>2.5</sub> Variability from 1959 to 2022**

### 832 **5.1 Monthly PM<sub>2.5</sub> and Trend**

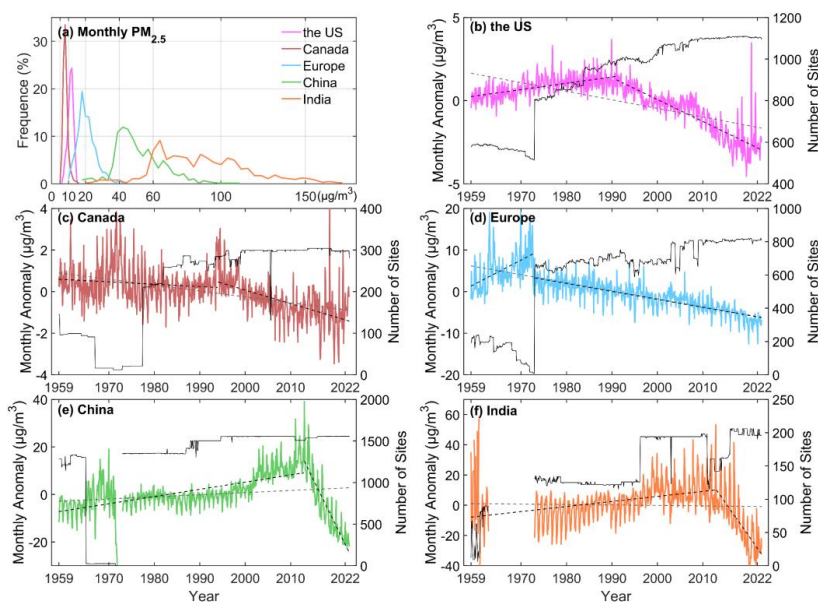
833 Figure 14 (a) shows the frequency of the estimated monthly PM<sub>2.5</sub> from 1959 to 2022, and Table 3  
834 lists the maximum frequency for each region. The order of the concentrations with the greatest  
835 frequency was Canada (8 µg/m<sup>3</sup>), the United States (12 µg/m<sup>3</sup>), Europe (18 µg/m<sup>3</sup>), China (42 µg/m<sup>3</sup>)  
836 and India (64 µg/m<sup>3</sup>). Canada and the United States are areas with less frequent PM<sub>2.5</sub> pollution.  
837 PM<sub>2.5</sub> pollution occurs frequently in China and India. The results indicate that the PM<sub>2.5</sub>  
838 concentrations in developed countries are significantly lower than those in developing countries in  
839 the Northern Hemisphere.

840 Figure 14 (b-f) shows the anomalies of the estimated monthly PM<sub>2.5</sub> concentration from 1959 to  
841 2022, and Table 3 lists the trends for each region. The trends in each region from 1959 to 2022 are  
842 all negative; however, the trend in India does not pass the significance test (p>0.05). The fastest  
843 downward trend is in Europe, at -1.93 µg/m<sup>3</sup>/decade. The trends in different regions vary at different  
844 times. Positive trends are detected in the United States from 1959 to 1990, in Canada from 1959 to  
845 1993, and in China and India from 1959 to 2012. The most rapid upward trend is observed in India,  
846 at 3.35 µg/m<sup>3</sup>/decade from 1959 to 2012. Negative trends are detected in the United States from  
847 1991 to 2022, in Europe from 1959 to 1972 and from 1973 to 2022, and in China and India from  
848 2013 to 2022. The most significant downward trend is observed in India, at -42.84 µg/m<sup>3</sup>/decade.  
849 These regional trends are similar to those of previous studies in different periods (Van Donkelaar et  
850 al., 2010; Wang et al., 2012; Boys et al., 2014; Ma et al., 2016; Li et al., 2017; Hammer et al., 2020).

851 The trends in PM<sub>2.5</sub> concentration changes in different regions are closely associated with the  
852 implementation of relevant policies. The earlier pollution control measures are taken, the earlier the  
853 decreasing trend in the PM<sub>2.5</sub> concentration occurs, and the lower the threat of particulate matter  
854 pollution is to humans. In 1997, the United States EPA classified PM<sub>2.5</sub> as a hazardous substance  
855 in the National Ambient Air Quality Standard, and subsequent regulations in 2006 further  
856 strengthened the source control and management of fine particulate matter (Gilliam and Hall, 2016).  
857 In 1988, the Canadian federal government enacted the Canadian Environmental Protection Act,  
858 which enhanced the regulation of PM<sub>2.5</sub> (Davies, 1988). The European Union introduced the Air  
859 Quality Directive in 1996, followed by multiple revisions and updates to regulate and restrict air



860 pollutants, including  $PM_{2.5}$  (Kuklinska et al., 2015). However, Europe stands out due to its early  
 861 adoption of clean production practices in heavy industries since the 1970s. Since 2012, China has  
 862 implemented numerous regulations and standards for  $PM_{2.5}$ . For instance, the Monitoring Method  
 863 for Atmospheric Particulate Matter ( $PM_{2.5}$ ) was issued in 2012, and the Chinese Ministry of  
 864 Environmental Protection released the Ambient Air Quality Standards in 2013, which include  
 865 emission standards for  $PM_{2.5}$  (Zhao et al., 2016a). In 2009, the Indian Ministry of Environment and  
 866 Forests issued the National Ambient Air Quality Standards, which include control standards for air  
 867 pollutants, including  $PM_{2.5}$ . Since 2015, the Indian government launched the National Clean Air  
 868 Programme (NCAP) to improve air quality in India by implementing a series of measures to reduce  
 869 the emissions of  $PM_{2.5}$  and other pollutants (Ganguly et al., 2020). These environmental regulations  
 870 have contributed significantly to the decline in  $PM_{2.5}$  concentrations.



871

872 **Figure 14** Frequency (a) and anomalies (b-f) of monthly  $PM_{2.5}$  from 1959 to 2022 in the United  
 873 States (the US), Canada, Europe, China, and India. The right Y-axis (b-f) is the monthly number of  
 874 sites.

875 **Table 3** The frequency and trend of the monthly  $PM_{2.5}$  concentration from 1959 to 2022 in the  
 876 United States (the US), Canada, Europe, China and India.

	Concentration Mode ( $\mu\text{g}/\text{m}^3$ ) and maximum frequency (%)	Trend ( $\mu\text{g}/\text{m}^3/\text{decade}$ )		
the US	12 (24.3%)	-0.52* (1959-2022)	0.38* (1959-1990)	-1.32* (1991-2022)
Canada	8 (33.5%)	-0.28* (1959-2022)	-0.11* (1959-1993)	-6.48* (1994-2022)
Europe	18 (19.4%)	-1.93* (1959-2022)	5.69* (1959-1972)	-1.91* (1973-2022)
China	42 (11.9%)	-0.89*	3.04*	-38.82*



		(1959-2022)	(1959-2012)	(2013-2022)
<i>India</i>	64 (9.1%)	-0.31	3.35*	-42.84*
		(1959-2022)	(1959-2012)	(2013-2022)

877 The symbol \* indicates passing the significance test,  $p < 0.01$ ; otherwise, not passing the significance  
 878 test,  $p > 0.05$ .

## 879 5.2 Annual $PM_{2.5}$ and Distribution

880 We analyze the spatial distribution of the multiyear average  $PM_{2.5}$  concentration in each region, and  
 881 we investigate the yearly variations in the spatial distribution based on the SDE and the average  
 882 center, as shown in Figure 15. The mean center and SDE describe the periodic changes in the spatial  
 883 distribution and dispersion of the  $PM_{2.5}$  concentration in each region. The larger the ellipse area is,  
 884 the more dispersed the spatial distribution of  $PM_{2.5}$  is. The flatter the ellipse is, the stronger the  
 885 spatial correlation of  $PM_{2.5}$ , and the direction of the major axis indicates the direction of the  
 886 concentration.

887 The multiyear average  $PM_{2.5}$  concentrations from 1959 to 2022 are  $11.2 \mu\text{g}/\text{m}^3$  in the United States,  
 888  $8.2 \mu\text{g}/\text{m}^3$  in Canada,  $20.1 \mu\text{g}/\text{m}^3$  in Europe,  $51.3 \mu\text{g}/\text{m}^3$  in China, and  $88.6 \mu\text{g}/\text{m}^3$  in India.  $PM_{2.5}$   
 889 concentrations in developed regions (North America and Europe) are significantly lower than those  
 890 in developing regions (China and India).

891 For the United States, the concentration in the eastern region is greater than that in the western  
 892 region. The  $PM_{2.5}$  concentration at most sites in the eastern region is greater than  $10 \mu\text{g}/\text{m}^3$ . Based  
 893 on the area of the SDE, the spatial distribution is divided into three stages: 1959-1972, 1973-1976,  
 894 and 1977-2022. The area decreases and then increases, indicating a changing trend in the spatial  
 895 extent of the  $PM_{2.5}$  concentration. The concentration distribution direction is east–west and rotates  
 896 northward, and the mean center gradually moves northwest after 1977, indicating an increase in the  
 897  $PM_{2.5}$  contribution in the western region.

898 For Canada, the concentrations in the eastern and western regions are greater than those in the  
 899 central region. The area of the ellipse increases and then decreases. The concentration distribution  
 900 direction is northwest-to-southeast, and the concentration rotates southward after 1977, indicating  
 901 an increase in weight in the western region. The mean center gradually moves northwestward and  
 902 then southeastward.

903 For Europe, high-concentration areas are mainly located in the central and eastern regions. The  
 904 ellipse's area can be divided into three stages: 1959-1967, 1968-1972, and 1973-2022. The spatial  
 905 variability decreases and then increases, corresponding to the mean centers moving north, south,  
 906 and north. The concentration direction is northwest–southeast, and the major axis shortens after  
 907 1993, indicating that the directionality of the concentration weakens.

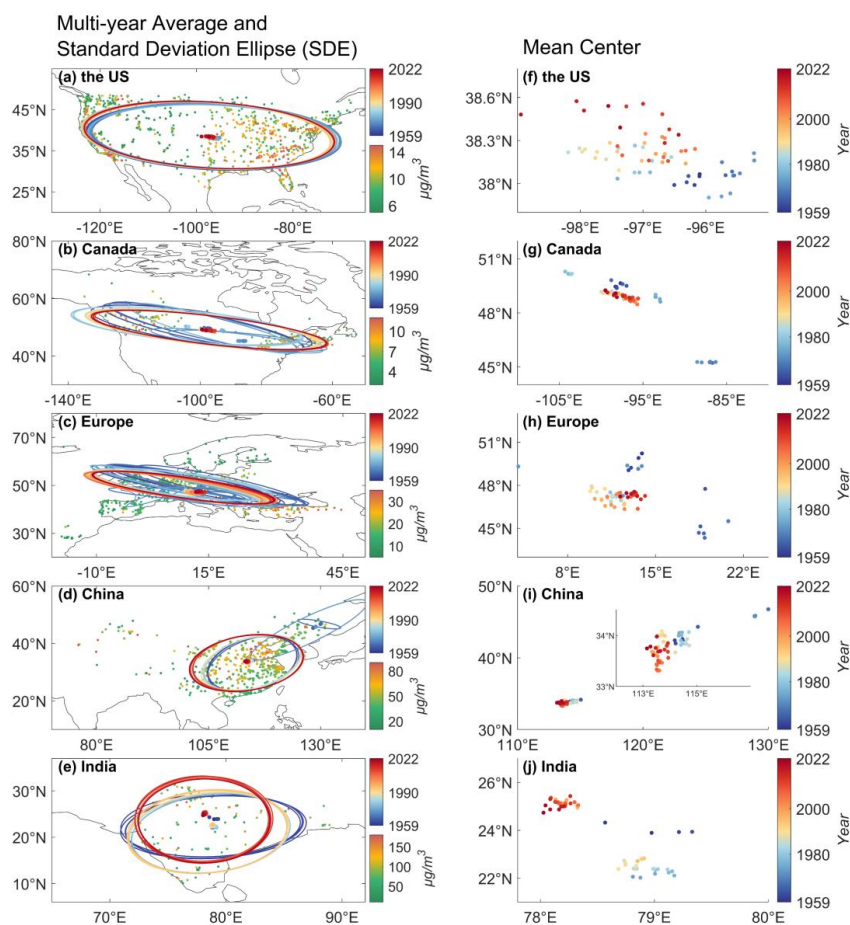
908 For China, high-concentration areas are in the central and eastern regions. The center of the SDE is  
 909 located in the northeast region from 1965 to 1971, which may be related to Northeast China being  
 910 the center of heavy industry during that period. After 1988, the area of the SDE increases  
 911 significantly, and the center moves significantly southwestward and gradually northward after 2008.  
 912 This finding indicates that the spatial distribution of  $PM_{2.5}$  increases in a discrete pattern after 1988,  
 913 and the concentration weight in the eastern region gradually increases. After 2008, the weight in the  
 914 western region decreases again.



915 For India, the highest concentration is in the northern region, and the lowest concentration is in the  
916 southern region. The area, shape, and mean center of the SDE show significant changes and can be  
917 divided into three stages. The SDE flattens between 1959 and 1962. The flattening weakens, and  
918 the area increases from 1963 to 1995. The spatial variability in  $PM_{2.5}$  increases, and the mean center  
919 moves southward. From 1996 to 2022, the flattening further weakens, the area decreases, the spatial  
920 variability in  $PM_{2.5}$  decreases, and the mean center shifts northward.

921 Above all, the concentration distributions in the United States and India exhibit an east–west pattern.  
922 The concentration distribution in Canada and Europe shows a northwest-to-southeast concentration  
923 gradient. In China, the  $PM_{2.5}$  concentration distribution ranges from northeast to southwest. There  
924 are strong correlations between the  $PM_{2.5}$  concentration and the location of the sites in Europe and  
925 Canada. However, the spatial correlation in India is gradually weakening, and the spatial dispersion  
926 of  $PM_{2.5}$  in China is increasing. Studies have shown that the variation in  $PM_{2.5}$  based on the mean  
927 center and the SDE is related to several factors, such as the energy structure, urbanization process,  
928 population distribution and vegetation coverage (Shi et al., 2018; Wu et al., 2018; Li et al., 2019;  
929 Wang et al., 2019; Lim et al., 2020; Qi et al., 2023).





930

931 **Figure 15** The spatial distribution of the multiyear average and standard deviation ellipse (SDE) (a-  
932 e) and the mean center (f-j) of the  $PM_{2.5}$  concentration from 1959 to 2022 in the United States (the  
933 US), Canada, Europe, China, and India. The mean center and SDE describe the changes in the spatial  
934 distribution. The larger the ellipse area is, the more dispersed the spatial distribution of  $PM_{2.5}$  is.  
935 The flatter the ellipse is, the stronger the spatial correlation of  $PM_{2.5}$  is. The direction of the major axis  
936 indicates the direction of the concentration.

## 937 6 Conclusions

938 This study uses a machine learning method to estimate daily  $PM_{2.5}$  for 4011 terrestrial sites in the  
939 Northern Hemisphere from 1959 to 2022 based on hourly visibility and related meteorological  
940 variables. Eighty percent of the sample data are used to train the model, and 20% are used for testing.  
941 The model's performance and predictive ability are evaluated. We analyze the uncertainty and  
942 discuss the limitations of the dataset. We compare the estimated  $PM_{2.5}$  with the  $PM_{2.5}$  based on the  
943 satellite AOD and  $PM_{2.5}$  of the reanalysis datasets. Finally, the  $PM_{2.5}$  variability in each region over  
944 the past 64 years is analyzed. We hope our dataset will be useful for studying the atmospheric



945 environment, human health, and climate change and provide auxiliary support for assimilation.  
946 Several key results of this study are described as follows:

947 **The most important variable** Visibility is the most important variable at 79.1% of the PM<sub>2.5</sub> sites,  
948 as visibility can also be considered an indicator of PM<sub>2.5</sub> without fog or precipitation. Other  
949 meteorological variables play a secondary role in the model, especially temperature and dew point  
950 temperature. Visibility can serve as a good indicator of PM<sub>2.5</sub>.

951 **Model performance and predictive ability.** The training results show that the slope between the  
952 estimated PM<sub>2.5</sub> concentration and the monitored PM<sub>2.5</sub> concentration within the 95% confidence  
953 interval is 0.946, the R<sup>2</sup> is 0.95, the RMSE is 7.0 µg/m<sup>3</sup>, and the MAE is 3.1 µg/m<sup>3</sup>. The test results  
954 show that the slope between the predicted PM<sub>2.5</sub> concentration and the monitored PM<sub>2.5</sub>  
955 concentration is 0.862 ± 0.0010 within a 95% confidence interval, R<sup>2</sup> is 0.80, RMSE is 13.5 µg/m<sup>3</sup>,  
and MAE is 6.9 µg/m<sup>3</sup>. The model shows good stability and predictive ability.

957 **Comparison with other datasets.** The estimated PM<sub>2.5</sub> concentration is consistent with the PM<sub>2.5</sub>  
958 concentration based on satellite AOD data at the monthly scale. The correlation coefficient of the  
959 annual cycles in each region is greater than 0.96. Compared with the reanalysis data, there are some  
960 differences among regions, which are closely related to the accuracy of emission inventories and  
961 the vertical structures of aerosols.

962 **Monthly PM<sub>2.5</sub>.** From 1959 to 2022, the PM<sub>2.5</sub> concentration at the highest frequency is 12 µg/m<sup>3</sup>,  
963 8 µg/m<sup>3</sup>, 17 µg/m<sup>3</sup>, 40 µg/m<sup>3</sup> and 63 µg/m<sup>3</sup>, and the trends are -0.52 µg/m<sup>3</sup>/decade, -0.28  
964 µg/m<sup>3</sup>/decade, -1.93 µg/m<sup>3</sup>/decade, -0.89 µg/m<sup>3</sup>/decade, and -0.31 µg/m<sup>3</sup>/decade, respectively, for  
965 the United States, Canada, Europe, China, and India. PM<sub>2.5</sub> concentrations in all regions show a  
966 periodic increase and decrease from 1959 to 2022. The decreasing trends are -1.32 µg/m<sup>3</sup>/decade  
967 from 1991 to 2022 in the United States, -6.48 µg/m<sup>3</sup>/decade from 1994 to 2022 in Canada, -1.91  
968 µg/m<sup>3</sup>/decade from 1973 to 2022 in Europe, and -38.82 µg/m<sup>3</sup>/decade and -42.84 µg/m<sup>3</sup>/decade from  
969 2013 to 2022 in China and India, respectively. Although the PM<sub>2.5</sub> concentrations in developing  
970 countries are significantly greater than those in developed countries, they have declined more  
971 quickly in recent years.

972 **Annual PM<sub>2.5</sub>.** The multiyear average PM<sub>2.5</sub> concentrations from 1959 to 2022 in the United States,  
973 Canada, Europe, China, and India are 11.2 µg/m<sup>3</sup>, 8.2 µg/m<sup>3</sup>, 20.1 µg/m<sup>3</sup>, 51.3 µg/m<sup>3</sup> and 88.6 µg/m<sup>3</sup>,  
974 respectively. Based on the features of the SDE and mean center, the spatial distribution of PM<sub>2.5</sub> has  
975 more spatial variability in the United States, Canada, and Europe and less variability in China and  
976 India. The changes in the mean center of the PM<sub>2.5</sub> concentration exhibit various patterns in each  
977 region.

## 978 **7 Data Availability**

979 Daily PM<sub>2.5</sub> concentration data at 4011 sites in the Northern Hemisphere from 1959 to 2022 are  
980 available at <https://cstr.cn/18406.11.Atmos.tpsc.301127> (Hao et al., 2024).

## 981 **Competing Interests**

982 The contact author has declared that none of the authors has any competing interests.

## 983 **Acknowledgments**



984 This work was supported by the National Key Research & Development Program of China  
985 (2022YFF0801302) and the National Natural Science Foundation of China (41930970). The hourly  
986 visibility data are available at from <https://mesonet.agron.iastate.edu/ASOS/>. The hourly PM<sub>2.5</sub> data  
987 for the United States are available at <https://www.epa.gov/aqs>. The hourly PM<sub>2.5</sub> data for Canada  
988 are available at <https://www.canada.ca>. The hourly PM<sub>2.5</sub> data for Europe available at  
989 <https://european-union.europa.eu>. The hourly PM<sub>2.5</sub> data for China are available at  
990 <https://www.cnemc.cn>. The hourly PM<sub>2.5</sub> data for India are available at <https://app.cpcbcr.com>. The  
991 hourly visibility and meteorological data are available at <https://www.weather.gov/asos>. The  
992 monthly global PM<sub>2.5</sub> dataset for the Atmospheric Composition Analysis Group version V5.GL.04  
993 (ACAG) are available at <https://sites.wustl.edu/acag/datasets/surface-pm2-5/>. The monthly PM<sub>2.5</sub>  
994 dataset of China High Air Pollutants (CHAP) are available at <https://zenodo.org/records/6398971>.  
995 The monthly PM<sub>2.5</sub> dataset of Modern-Era Retrospective Analysis for Research and Applications,  
996 version 2 (MERRA-2) are available at <https://gmao.gsfc.nasa.gov>. The monthly PM<sub>2.5</sub> of the  
997 Copernicus Atmosphere Monitoring Service (CAMS) reanalysis are available at  
998 <https://ads.atmosphere.copernicus.eu/cdsapp#!/dataset/cams-global-reanalysis-eac4>.

999

1000

1001

## 1002 **References**

- 1003 Albrecht, B. A.: Aerosols, cloud microphysics, and fractional cloudiness, *Science*, 245, 1227-1230,  
1004 <https://doi.org/10.1126/science.245.4923.1227>, 1989.
- 1005 Ali, M. A., Bilal, M., Wang, Y., Nichol, J. E., Mhawish, A., Qiu, Z., de Leeuw, G., Zhang, Y., Zhan, Y.,  
1006 Liao, K., Almazroui, M., Dambul, R., Shahid, S., and Islam, M. N.: Accuracy assessment of CAMS and  
1007 MERRA-2 reanalysis PM<sub>2.5</sub> and PM<sub>10</sub> concentrations over China, *Atmos. Environ.*, 288, 119297,  
1008 <https://doi.org/10.1016/j.atmosenv.2022.119297>, 2022.
- 1009 Beckerman, B. S., Jerrett, M., Serre, M., Martin, R. V., Lee, S.-J., Van Donkelaar, A., Ross, Z., Su, J.,  
1010 and Burnett, R. T.: A hybrid approach to estimating national scale spatiotemporal variability of PM<sub>2.5</sub>  
1011 in the contiguous United States, *Environ. Sci. Technol.*, 47, 7233-7241,  
1012 <https://doi.org/10.1021/es400039u>, 2013.
- 1013 Benedetti, A., Morcrette, J.-J., Boucher, O., Dethof, A., Engelen, R. J., Fisher, M., Flentje, H., Huneeus,  
1014 N., Jones, L., Kaiser, J. W., Kinne, S., Mangold, A., Razinger, M., Simmons, A. J., and Suttie, M.: Aerosol  
1015 analysis and forecast in the European Centre for Medium-Range Weather Forecasts Integrated Forecast  
1016 System: 2. Data assimilation, *J. Geophys. Res.-Atmos.*, 114, <https://doi.org/10.1029/2008JD011115>, 2009.
- 1017 Bergstrom, R. W., Pilewskie, P., Russell, P. B., Redemann, J., Bond, T. C., Quinn, P. K., and Sierau, B.:  
1018 Spectral absorption properties of atmospheric aerosols, *Atmos. Chem. Phys.*, 7, 5937-5943,  
1019 <https://doi.org/10.5194/acp-7-5937-2007>, 2007.
- 1020 Boers, R., van Weele, M., van Meijgaard, E., Savenije, M., Siebesma, A. P., Bosveld, F., and Stammes,  
1021 P.: Observations and projections of visibility and aerosol optical thickness (1956-2100) in the  
1022 Netherlands: impacts of time-varying aerosol composition and hygroscopicity, *Environ. Res. Lett.*, 10,  
1023 <https://doi.org/10.1088/1748-9326/10/1/015003>, 2015.
- 1024 Boys, B., Martin, R., Van Donkelaar, A., MacDonell, R., Hsu, N., Cooper, M., Yantosca, R., Lu, Z.,  
1025 Streets, D., and Zhang, Q.: Fifteen-year global time series of satellite-derived fine particulate matter,



- 1026 Environ. Sci. Technol., 48, 11109-11118, <https://doi.org/10.1021/es502113p>, 2014.
- 1027 Browne, M. W.: Cross-validation methods, *J. Math. Psychol.*, 44, 108-132,
- 1028 <https://doi.org/10.1006/jmps.1999.1279>, 2000.
- 1029 Buchard, V., da Silva, A. M., Colarco, P. R., Darmenov, A., Randles, C. A., Govindaraju, R., Torres, O.,
- 1030 Campbell, J., and Spurr, R.: Using the OMI aerosol index and absorption aerosol optical depth to evaluate
- 1031 the NASA MERRA Aerosol Reanalysis, *Atmos. Chem. Phys.*, 15, 5743-5760,
- 1032 <https://doi.org/10.5194/acp-15-5743-2015>, 2015.
- 1033 Buchard, V., da Silva, A. M., Randles, C. A., Colarco, P., Ferrare, R., Hair, J., Hostetler, C., Tackett, J.,
- 1034 and Winker, D.: Evaluation of the surface PM<sub>2.5</sub> in Version 1 of the NASA MERRA Aerosol Reanalysis
- 1035 over the United States, *Atmos. Environ.*, 125, 100-111, <https://doi.org/10.1016/j.atmosenv.2015.11.004>,
- 1036 2016.
- 1037 Buchard, V., Randles, C. A., da Silva, A. M., Darmenov, A., Colarco, P. R., Govindaraju, R., Ferrare, R.,
- 1038 Hair, J., Beyersdorf, A. J., Ziemba, L. D., and Yu, H.: The MERRA-2 Aerosol Reanalysis, 1980 Onward.
- 1039 Part II: Evaluation and Case Studies, *J. Climate*, 30, 6851-6872, [https://doi.org/10.1175/JCLI-D-16-](https://doi.org/10.1175/JCLI-D-16-0613.1)
- 1040 [0613.1](https://doi.org/10.1175/JCLI-D-16-0613.1), 2017.
- 1041 Chafe, Z. A., Brauer, M., Klimont, Z., Van Dingenen, R., Mehta, S., Rao, S., Riahi, K., Dentener, F., and
- 1042 Smith, K. R.: Household Cooking with Solid Fuels Contributes to Ambient PM<sub>2.5</sub> Air Pollution and the
- 1043 Burden of Disease, *Environ. Health Persp.*, 122, 1314-1320, <https://doi.org/10.1289/ehp.1206340>, 2014.
- 1044 Che, H., Xia, X., Zhu, J., Hong, W., and Shi, G.: Aerosol optical properties under the condition of heavy
- 1045 haze over an urban site of Beijing, China, *Environ. Sci. Pollut. R.*, 22, 1043-1053,
- 1046 <https://doi.org/10.1007/s11356-014-3415-5>, 2014.
- 1047 Chen, A., Zhao, C., and Fan, T.: Spatio-temporal distribution of aerosol direct radiative forcing over mid-
- 1048 latitude regions in north hemisphere estimated from satellite observations, *Atmos. Res.*, 266, 105938,
- 1049 <https://doi.org/10.1016/j.atmosres.2021.105938>, 2022.
- 1050 Chen, Z., Chen, D., Zhao, C., Kwan, M.-p., Cai, J., Zhuang, Y., Zhao, B., Wang, X., Chen, B., Yang, J.,
- 1051 Li, R., He, B., Gao, B., Wang, K., and Xu, B.: Influence of meteorological conditions on
- 1052 PM<sub><sub>2.5</sub></sub> concentrations across China: A review of methodology and mechanism, *Environ.*
- 1053 *Int.*, 139, <https://doi.org/10.1016/j.envint.2020.105558>, 2020.
- 1054 Chow, J. C., Doraiswamy, P., Watson, J. G., Chen, L. W. A., Ho, S. S. H., and Sodeman, D. A.: Advances
- 1055 in Integrated and Continuous Measurements for Particle Mass and Chemical Composition, *Journal of the*
- 1056 *Air & Waste Management Association*, 58, 141-163, <https://doi.org/10.3155/1047-3289.58.2.141>, 2008.
- 1057 Cohen, A. J., Brauer, M., Burnett, R., Anderson, H. R., Frostad, J., Estep, K., Balakrishnan, K.,
- 1058 Brunekreef, B., Dandona, L., Dandona, R., Feigin, V., Freedman, G., Hubbell, B., Jobling, A., Kan, H.,
- 1059 Knibbs, L., Liu, Y., Martin, R., Morawska, L., Pope, C. A., III, Shin, H., Straif, K., Shaddick, G., Thomas,
- 1060 M., van Dingenen, R., van Donkelaar, A., Vos, T., Murray, C. J. L., and Forouzanfar, M. H.: Estimates
- 1061 and 25-year trends of the global burden of disease attributable to ambient air pollution: an analysis of
- 1062 data from the Global Burden of Diseases Study 2015, *Lancet*, 389, 1907-1918,
- 1063 [https://doi.org/10.1016/s0140-6736\(17\)30505-6](https://doi.org/10.1016/s0140-6736(17)30505-6), 2017.
- 1064 Dabek-Zlotorzynska, E., Dann, T. F., Martinelango, P. K., Celso, V., Brook, J. R., Mathieu, D., Ding, L.,
- 1065 and Austin, C. C.: Canadian National Air Pollution Surveillance (NAPS) PM<sub><sub>2.5</sub></sub> speciation
- 1066 program: Methodology and PM<sub><sub>2.5</sub></sub> chemical composition for the years 2003-2008, *Atmos.*
- 1067 *Environ.*, 45, 673-686, <https://doi.org/10.1016/j.atmosenv.2010.10.024>, 2011.
- 1068 Davies, J.: CEPA—The Canadian. Environmental Protection Act, *JAPCA*, 38, 1111-1113,
- 1069 <https://doi.org/10.1080/08940630.1988.10466452>, 1988.



- 1070 Demerjian, K. L.: A review of national monitoring networks in North America, *Atmos. Environ.*, 34,  
1071 1861-1884, [https://doi.org/10.1016/S1352-2310\(99\)00452-5](https://doi.org/10.1016/S1352-2310(99)00452-5), 2000.
- 1072 Fan, H., Zhao, C., Yang, Y., and Yang, X.: Spatio-Temporal Variations of the  
1073  $PM_{2.5}/PM_{10}$  Ratios and Its Application to Air Pollution Type Classification  
1074 in China, *Front. Environ. Sci.*, 9, <https://doi.org/10.3389/fenvs.2021.692440>, 2021.
- 1075 Fei, Y., Liao, J., and Zhang, Z.: Consistency and Discrepancy between Visibility and  $PM_{2.5}$   
1076 Measurements: Potential Application of Visibility Observation to Air Quality Study, *Sensors*, 23, 898,  
1077 <https://doi.org/10.3390/s23020898>, 2023.
- 1078 Flemming, J., Huijnen, V., Arteta, J., Bechtold, P., Beljaars, A., Blechschmidt, A. M., Diamantakis, M.,  
1079 Engelen, R. J., Gaudel, A., Inness, A., Jones, L., Josse, B., Katragkou, E., Marecal, V., Peuch, V. H.,  
1080 Richter, A., Schultz, M. G., Stein, O., and Tsikerdekis, A.: Tropospheric chemistry in the Integrated  
1081 Forecasting System of ECMWF, *Geosci. Model Dev.*, 8, 975-1003, [https://doi.org/10.5194/gmd-8-975-](https://doi.org/10.5194/gmd-8-975-2015)  
1082 [2015](https://doi.org/10.5194/gmd-8-975-2015), 2015.
- 1083 Friedman, J. H.: Greedy function approximation: A gradient boosting machine, *Ann. Stat.*, 29, 1189-1232,  
1084 <https://doi.org/10.1214/aos/1013203451>, 2001.
- 1085 Ganguly, T., Selvaraj, K. L., and Guttikunda, S. K.: National Clean Air Programme (NCAP) for Indian  
1086 cities: Review and outlook of clean air action plans, *Atmospheric Environment X*, 8, 100096,  
1087 <https://doi.org/10.1016/j.aeaoa.2020.100096>, 2020.
- 1088 Gelaro, R., McCarty, W., Suárez, M. J., Todling, R., Molod, A., Takacs, L., Randles, C. A., Darmenov,  
1089 A., Bosilovich, M. G., Reichle, R., Wargan, K., Coy, L., Cullather, R., Draper, C., Akella, S., Buchard,  
1090 V., Conaty, A., da Silva, A. M., Gu, W., Kim, G.-K., Koster, R., Lucchesi, R., Merkova, D., Nielsen, J.  
1091 E., Partyka, G., Pawson, S., Putman, W., Rienecker, M., Schubert, S. D., Sienkiewicz, M., and Zhao, B.:  
1092 The Modern-Era Retrospective Analysis for Research and Applications, Version 2 (MERRA-2), *J.*  
1093 *Climate*, 30, 5419-5454, <https://doi.org/10.1175/JCLI-D-16-0758.1>, 2017.
- 1094 Gilliam, J. and Hall, E.: Reference and Equivalent Methods Used to Measure National Ambient Air  
1095 Quality Standards (NAAQS) Criteria Air Pollutants-Volume I US Environmental Protection Agency,  
1096 Washington, DC, Environmental Protection Agency: Washington, DC, USA, 2016.
- 1097 Gong, J.: Clarifying the standard deviational ellipse, *Geogr. Anal.*, 34, 155-167,  
1098 <https://doi.org/10.1111/j.1538-4632.2002.tb01082.x>, 2002.
- 1099 Granier, C., Bessagnet, B., Bond, T., D'Angiola, A., Denier van der Gon, H., Frost, G. J., Heil, A., Kaiser,  
1100 J. W., Kinne, S., and Klimont, Z.: Evolution of anthropogenic and biomass burning emissions of air  
1101 pollutants at global and regional scales during the 1980–2010 period, *Climatic Change*, 109, 163-190,  
1102 <https://doi.org/10.1007/s10584-011-0154-1>, 2011.
- 1103 Green, D. and Fuller, G. W.: The implications of tapered element oscillating microbalance (TEOM)  
1104 software configuration on particulate matter measurements in the UK and Europe, *Atmos. Environ.*, 40,  
1105 5608-5616, <https://doi.org/10.1016/j.atmosenv.2006.04.052>, 2006.
- 1106 Guenther, A., Karl, T., Harley, P., Wiedinmyer, C., Palmer, P. I., and Geron, C.: Estimates of global  
1107 terrestrial isoprene emissions using MEGAN (Model of Emissions of Gases and Aerosols from Nature),  
1108 *Atmos. Chem. Phys.*, 6, 3181-3210, <https://doi.org/10.5194/acp-6-3181-2006>, 2006.
- 1109 Gui, K., Che, H., Zeng, Z., Wang, Y., Zhai, S., Wang, Z., Luo, M., Zhang, L., Liao, T., and Zhao, H.:  
1110 Construction of a virtual  $PM_{2.5}$  observation network in China based on high-density surface  
1111 meteorological observations using the Extreme Gradient Boosting model, *Environ. Int.*, 141, 105801,  
1112 <https://doi.org/10.1016/j.envint.2020.105801>, 2020.
- 1113 Guo, S., Hu, M., Zamora, M. L., Peng, J., Shang, D., Zheng, J., Du, Z., Wu, Z., Shao, M., Zeng, L.,



- 1114 Molina, M. J., and Zhang, R.: Elucidating severe urban haze formation in China, *P. Natl. A. Sci.*, 111,  
1115 17373-17378, <https://doi.org/10.1073/pnas.1419604111>, 2014.
- 1116 Hammer, M. S., van Donkelaar, A., Li, C., Lyapustin, A., Sayer, A. M., Hsu, N. C., Levy, R. C., Garay,  
1117 M. J., Kalashnikova, O. V., and Kahn, R. A.: Global estimates and long-term trends of fine particulate  
1118 matter concentrations (1998–2018), *Environ. Sci. Technol.*, 54, 7879-7890,  
1119 <https://doi.org/10.1021/acs.est.0c01764>, 2020.
- 1120 Hao, H., Wang, K., Wu, G., Liu, J., and Li, J.: PM<sub>2.5</sub> concentrations based on near-surface visibility at  
1121 4011 sites in the Northern Hemisphere from 1959 to 2022, National Tibetan Plateau Data Center [dataset],  
1122 <https://doi.org/10.11888/Atmos.tpd.c.301127>, 2024.
- 1123 He, Q., Gao, K., Zhang, L., Song, Y., and Zhang, M.: Satellite-derived 1-km estimates and long-term  
1124 trends of PM<sub>2.5</sub> concentrations in China from 2000 to 2018, *Environ. Int.*, 156, 106726,  
1125 <https://doi.org/10.1016/j.envint.2021.106726>, 2021.
- 1126 Hsu, N., Lee, J., Sayer, A., Carletta, N., Chen, S. H., Tucker, C., Holben, B., and Tsay, S. C.: Retrieving  
1127 near-global aerosol loading over land and ocean from AVHRR, *J. Geophys. Res-Atmos.*, 122, 9968-9989,  
1128 <https://doi.org/10.1002/2017JD026932>, 2017.
- 1129 Huang, W., Tan, J., Kan, H., Zhao, N., Song, W., Song, G., Chen, G., Jiang, L., Jiang, C., and Chen, R.:  
1130 Visibility, air quality and daily mortality in Shanghai, China, *Sci. Total Environ.*, 407, 3295-3300,  
1131 <https://doi.org/10.1016/j.scitotenv.2009.02.019>, 2009.
- 1132 Huijnen, V., Pozzer, A., Arteta, J., Brasseur, G., Bouarar, I., Chabrillat, S., Christophe, Y., Doumbia, T.,  
1133 Flemming, J., Guth, J., Josse, B., Karydis, V. A., Marécal, V., and Pelletier, S.: Quantifying uncertainties  
1134 due to chemistry modelling – evaluation of tropospheric composition simulations in the CAMS model  
1135 (cycle 43R1), *Geosci. Model Dev.*, 12, 1725-1752, <https://doi.org/10.5194/gmd-12-1725-2019>, 2019.
- 1136 Inness, A., Ades, M., Agustí-Panareda, A., Barré, J., Benedictow, A., Blechschmidt, A.-M., Dominguez,  
1137 J. J., Engelen, R., Eskes, H., and Flemming, J.: The CAMS reanalysis of atmospheric composition, *Atmos.*  
1138 *Chem. Phys.*, 19, 3515-3556, <https://doi.org/10.5194/acp-19-3515-2019>, 2019.
- 1139 Jaswal, A.: Changes in total cloud cover over India based upon 1961-2007 surface observations, *Mausam*,  
1140 61, 455-468, <https://doi.org/10.54302/mausam.v61i4.882>, 2010.
- 1141 Jaswal, A., Kore, P., and Singh, V.: Variability and trends in low cloud cover over India during 1961-  
1142 2010, *Mausam*, 68, 235-252, <https://doi.org/10.54302/mausam.v68i2.627>, 2017.
- 1143 Jaswal, A. K., Kumar, N., Prasad, A. K., and Kafatos, M.: Decline in horizontal surface visibility over  
1144 India (1961–2008) and its association with meteorological variables, *Nat. hazards*, 68, 929-954,  
1145 <https://doi.org/10.1007/s11069-013-0666-2>, 2013.
- 1146 Jin, C., Wang, Y., Li, T., and Yuan, Q.: Global validation and hybrid calibration of CAMS and MERRA-  
1147 2 PM<sub>2.5</sub> reanalysis products based on OpenAQ platform, *Atmos. Environ.*, 274, 118972,  
1148 <https://doi.org/10.1016/j.atmosenv.2022.118972>, 2022.
- 1149 Kaiser, J. W., Heil, A., Andreae, M. O., Benedetti, A., Chubarova, N., Jones, L., Morcrette, J. J., Razinger,  
1150 M., Schultz, M. G., Suttie, M., and van der Werf, G. R.: Biomass burning emissions estimated with a  
1151 global fire assimilation system based on observed fire radiative power, *Biogeosciences*, 9, 527-554,  
1152 <https://doi.org/10.5194/bg-9-527-2012>, 2012.
- 1153 Kim, K.-H., Kabir, E., and Kabir, S.: A review on the human health impact of airborne particulate matter,  
1154 *Environ. Int.*, 74, 136-143, <https://doi.org/10.1016/j.envint.2014.10.005>, 2015.
- 1155 Kong, L., Tang, X., Zhu, J., Wang, Z., Li, J., Wu, H., Wu, Q., Chen, H., Zhu, L., Wang, W., Liu, B., Wang,  
1156 Q., Chen, D., Pan, Y., Song, T., Li, F., Zheng, H., Jia, G., Lu, M., Wu, L., and Carmichael, G. R.: A 6-  
1157 year-long (2013–2018) high-resolution air quality reanalysis dataset in China based on the assimilation



- 1158 of surface observations from CNEMC, *Earth Syst. Sci. Data*, 13, 529-570, <https://doi.org/10.5194/essd-13-529-2021>, 2021.
- 1160 Kuklinska, K., Wolska, L., and Namiesnik, J.: Air quality policy in the US and the EU—a review, *Atmos. Pollut. Res.*, 6, 129-137, <https://doi.org/10.5094/APR.2015.015>, 2015.
- 1162 Lelieveld, J., Evans, J. S., Fnais, M., Giannadaki, D., and Pozzer, A.: The contribution of outdoor air pollution sources to premature mortality on a global scale, *Nature*, 525, 367+, <https://doi.org/10.1038/nature15371>, 2015.
- 1165 Li, C., Martin, R. V., van Donkelaar, A., Boys, B. L., Hammer, M. S., Xu, J.-W., Marais, E. A., Reff, A., Strum, M., and Ridley, D. A.: Trends in chemical composition of global and regional population-weighted fine particulate matter estimated for 25 years, *Environ. Sci. Technol.*, 51, 11185-11195, <https://doi.org/10.1021/acs.est.7b02530>, 2017.
- 1169 Li, J., Han, X., Jin, M., Zhang, X., and Wang, S.: Globally analysing spatiotemporal trends of anthropogenic PM<sub>2.5</sub> concentration and population's PM<sub>2.5</sub> exposure from 1998 to 2016, *Environ. Int.*, 128, 46-62, <https://doi.org/10.1016/j.envint.2019.04.026>, 2019.
- 1172 Li, J., Garshick, E., Hart, J. E., Li, L., Shi, L., Al-Hemoud, A., Huang, S., and Koutrakis, P.: Estimation of ambient PM<sub>2.5</sub> in Iraq and Kuwait from 2001 to 2018 using machine learning and remote sensing, *Environ. Int.*, 151, <https://doi.org/10.1016/j.envint.2021.106445>, 2021.
- 1175 Li, J., Carlson, B. E., Yung, Y. L., Lv, D., Hansen, J., Penner, J. E., Liao, H., Ramaswamy, V., Kahn, R. A., Zhang, P., Dubovik, O., Ding, A., Lacis, A. A., Zhang, L., and Dong, Y.: Scattering and absorbing aerosols in the climate system, *Nat. Rev. Earth. Environ.*, 3, 363-379, <https://doi.org/10.1038/s43017-022-00296-7>, 2022.
- 1179 Li, S., Chen, L., Huang, G., Lin, J., Yan, Y., Ni, R., Huo, Y., Wang, J., Liu, M., and Weng, H.: Retrieval of surface PM<sub>2.5</sub> mass concentrations over North China using visibility measurements and GEOS-Chem simulations, *Atmos. Environ.*, 222, 117121, <https://doi.org/10.1016/j.atmosenv.2019.117121>, 2020.
- 1182 Liao, H., Chang, W., and Yang, Y.: Climatic Effects of Air Pollutants over China: A Review, *Adv. Atmos. Sci.*, 32, 115-139, <https://doi.org/10.1007/s00376-014-0013-x>, 2015.
- 1184 Lim, C.-H., Ryu, J., Choi, Y., Jeon, S. W., and Lee, W.-K.: Understanding global PM<sub>2.5</sub> concentrations and their drivers in recent decades (1998–2016), *Environ. Int.*, 144, 106011, <https://doi.org/10.1016/j.envint.2020.106011>, 2020.
- 1187 Liu, M., Bi, J., and Ma, Z.: Visibility-based PM<sub>2.5</sub> concentrations in China: 1957–1964 and 1973–2014, *Environ. Sci. Technol.*, 51, 13161-13169, <https://doi.org/10.1021/acs.est.7b03468>, 2017.
- 1189 Liu, M., Huang, X., Song, Y., Tang, J., Cao, J., Zhang, X., Zhang, Q., Wang, S., Xu, T., Kang, L., Cai, X., Zhang, H., Yang, F., Wang, H., Yu, J. Z., Lau, A. K. H., He, L., Huang, X., Duan, L., Ding, A., Xue, L., Gao, J., Liu, B., and Zhu, T.: Ammonia emission control in China would mitigate haze pollution and nitrogen deposition, but worsen acid rain, *P. Natl. A. Sci.*, 116, 7760-7765, <https://doi.org/10.1073/pnas.1814880116>, 2019.
- 1194 Liu, S., Geng, G., Xiao, Q., Zheng, Y., Liu, X., Cheng, J., and Zhang, Q.: Tracking daily concentrations of PM<sub>2.5</sub> chemical composition in China since 2000, *Environ. Sci. Technol.*, 56, 16517-16527, <https://doi.org/10.1021/acs.est.2c06510>, 2022.
- 1197 Ma, Z., Hu, X., Sayer, A. M., Levy, R., Zhang, Q., Xue, Y., Tong, S., Bi, J., Huang, L., and Liu, Y.: Satellite-based spatiotemporal trends in PM<sub>2.5</sub> concentrations: China, 2004–2013, *Environ. Health Persp.*, 124, 184-192, <https://doi.org/10.1289/ehp.1409481>, 2016.
- 1200 Mandal, S., Madhipatla, K. K., Guttikunda, S., Kloog, I., Prabhakaran, D., Schwartz, J. D., and Team, G. H. I.: Ensemble averaging based assessment of spatiotemporal variations in ambient PM<sub>2.5</sub>
- 1201



- 1202 concentrations over Delhi, India, during 2010–2016, *Atmos. Environ.*, 224, 117309,  
1203 <https://doi.org/10.1016/j.atmosenv.2020.117309>, 2020.
- 1204 Meng, X., Hand, J. L., Schichtel, B. A., and Liu, Y.: Space-time trends of PM<sub>2.5</sub> constituents in the  
1205 conterminous United States estimated by a machine learning approach, 2005–2015, *Environ. Int.*, 121,  
1206 1137–1147, <https://doi.org/10.1016/j.envint.2018.10.029>, 2018.
- 1207 Miao, Y. and Liu, S.: Linkages between aerosol pollution and planetary boundary layer structure in China,  
1208 *Sci. Total Environ.*, 650, 288–296, <https://doi.org/10.1016/j.scitotenv.2018.09.032>, 2019.
- 1209 Molnár, A., Mészáros, E., Imre, K., and Rüll, A.: Trends in visibility over Hungary between 1996 and  
1210 2002, *Atmos. Environ.*, 42, 2621–2629, <https://doi.org/10.1016/j.atmosenv.2007.05.012>, 2008.
- 1211 Nagaraja Rao, C., Stowe, L., and McClain, E.: Remote sensing of aerosols over the oceans using AVHRR  
1212 data Theory, practice and applications, *Int. J. Remote Sens.*, 10, 743–749,  
1213 <https://doi.org/10.1080/01431168908903915>, 1989.
- 1214 NOAA, DOD, FAA, and USN: Automated Surface Observing System (ASOS) User's Guide, 1998.
- 1215 Pant, P., Lal, R. M., Guttikunda, S. K., Russell, A. G., Nagpure, A. S., Ramaswami, A., and Peltier, R. E.:  
1216 Monitoring particulate matter in India: recent trends and future outlook, *Air Quality, Atmosphere &  
1217 Health*, 12, 45–58, <https://doi.org/10.1007/s11869-018-0629-6>, 2019.
- 1218 Provençal, S., Buchard, V., da Silva, A. M., Leduc, R., and Barrette, N.: Evaluation of PM surface  
1219 concentrations simulated by Version 1 of NASA's MERRA Aerosol Reanalysis over Europe, *Atmos.  
1220 Pollut. Res.*, 8, 374–382, <https://doi.org/10.1016/j.apr.2016.10.009>, 2017.
- 1221 Pui, D. Y. H., Chen, S.-C., and Zuo, Z.: PM<sub>2.5</sub> in China: Measurements, sources, visibility and health  
1222 effects, and mitigation, *Particuology*, 13, 1–26, <https://doi.org/10.1016/j.partic.2013.11.001>, 2014.
- 1223 Qi, G., Wei, W., Wang, Z., Wang, Z., and Wei, L.: The spatial-temporal evolution mechanism of PM<sub>2.5</sub>  
1224 concentration based on China's climate zoning, *J. Environ. Manage.*, 325, 116671,  
1225 <https://doi.org/10.1016/j.jenvman.2022.116671>, 2023.
- 1226 Ramanathan, V., Crutzen, P. J., Kiehl, J., and Rosenfeld, D.: Aerosols, climate, and the hydrological cycle,  
1227 *Science*, 294, 2119–2124, <https://doi.org/10.1126/science.1064034>, 2001.
- 1228 Ramanathan, V., Chung, C., Kim, D., Bettge, T., Buja, L., Kiehl, J. T., Washington, W. M., Fu, Q., Sikka,  
1229 D. R., and Wild, M.: Atmospheric brown clouds: Impacts on South Asian climate and hydrological cycle,  
1230 *P. Natl. A. Sci.*, 102, 5326–5333, <https://doi.org/10.1073/pnas.0500656102>, 2005.
- 1231 Randles, C. A., da Silva, A. M., Buchard, V., Colarco, P. R., Darmenov, A., Govindaraju, R., Smirnov,  
1232 A., Holben, B., Ferrare, R., Hair, J., Shinozuka, Y., and Flynn, C. J.: The MERRA-2 Aerosol Reanalysis,  
1233 1980 Onward. Part I: System Description and Data Assimilation Evaluation, *J. Climate*, 30, 6823–6850,  
1234 <https://doi.org/10.1175/JCLI-D-16-0609.1>, 2017.
- 1235 Ryu, Y.-H. and Min, S.-K.: Long-term evaluation of atmospheric composition reanalyses from CAMS,  
1236 TCR-2, and MERRA-2 over South Korea: Insights into applications, implications, and limitations,  
1237 *Atmos. Environ.*, 246, 118062, <https://doi.org/10.1016/j.atmosenv.2020.118062>, 2021.
- 1238 Samset, B. H., Lund, M. T., Bollasina, M., Myhre, G., and Wilcox, L.: Emerging Asian aerosol patterns,  
1239 *Nat. Geosci.*, 12, 582–584, <https://doi.org/10.1038/s41561-019-0424-5>, 2019.
- 1240 Shen, Z., Cao, J., Zhang, L., Zhang, Q., Huang, R.-J., Liu, S., Zhao, Z., Zhu, C., Lei, Y., and Xu, H.:  
1241 Retrieving historical ambient PM<sub>2.5</sub> concentrations using existing visibility measurements in Xi'an,  
1242 Northwest China, *Atmos. Environ.*, 126, 15–20, <https://doi.org/10.1016/j.atmosenv.2015.11.040>, 2016.
- 1243 Shi, Y., Matsunaga, T., Yamaguchi, Y., Li, Z., Gu, X., and Chen, X.: Long-term trends and spatial patterns  
1244 of satellite-retrieved PM<sub>2.5</sub> concentrations in South and Southeast Asia from 1999 to 2014, *Sci. Total  
1245 Environ.*, 615, 177–186, <https://doi.org/10.1016/j.scitotenv.2017.09.241>, 2018.





- 1246 Singh, A., Avis, W. R., and Pope, F. D.: Visibility as a proxy for air quality in East Africa, *Environ. Res.*  
1247 *Letts.*, 15, 084002, <https://doi.org/10.1088/1748-9326/ab8b12>, 2020.
- 1248 Su, L., Gao, C., Ren, X., Zhang, F., Cao, S., Zhang, S., Chen, T., Liu, M., Ni, B., and Liu, M.:  
1249 Understanding the spatial representativeness of air quality monitoring network and its application to  
1250 PM<sub>2.5</sub> in the mainland China, *Geoscience Frontiers*, 13, 101370,  
1251 <https://doi.org/10.1016/j.gsf.2022.101370>, 2022.
- 1252 Sun, E., Xu, X., Che, H., Tang, Z., Gui, K., An, L., Lu, C., and Shi, G.: Variation in MERRA-2 aerosol  
1253 optical depth and absorption aerosol optical depth over China from 1980 to 2017, *J. Atmos. Sol-Terr.*  
1254 *Phys.*, 186, 8-19, <https://doi.org/10.1016/j.jastp.2019.01.019>, 2019.
- 1255 Ukhov, A., Mostamandi, S., da Silva, A., Flemming, J., Alshehri, Y., Shevchenko, I., and Stenichkov, G.:  
1256 Assessment of natural and anthropogenic aerosol air pollution in the Middle East using MERRA-2,  
1257 CAMS data assimilation products, and high-resolution WRF-Chem model simulations, *Atmos. Chem.*  
1258 *Phys.*, 20, 9281-9310, <https://doi.org/10.5194/acp-20-9281-2020>, 2020.
- 1259 Van Donkelaar, A., Martin, R. V., and Park, R. J.: Estimating ground-level PM<sub>2.5</sub> using aerosol optical  
1260 depth determined from satellite remote sensing, *J. Geophys. Res.*, 111,  
1261 <https://doi.org/10.1029/2005JD006996>, 2006.
- 1262 Van Donkelaar, A., Martin, R. V., Brauer, M., and Boys, B. L.: Use of satellite observations for long-term  
1263 exposure assessment of global concentrations of fine particulate matter, *Environ. Health Persp.*, 123,  
1264 135-143, <https://doi.org/10.1289/ehp.1408646>, 2015.
- 1265 Van Donkelaar, A., Martin, R. V., Li, C., and Burnett, R. T.: Regional estimates of chemical composition  
1266 of fine particulate matter using a combined geoscience-statistical method with information from satellites,  
1267 models, and monitors, *Environ. Sci. Technol.*, 53, 2595-2611, <https://doi.org/10.1021/acs.est.8b06392>,  
1268 2019.
- 1269 Van Donkelaar, A., Martin, R. V., Brauer, M., Kahn, R., Levy, R., Verduzco, C., and Villeneuve, P. J.:  
1270 Global estimates of ambient fine particulate matter concentrations from satellite-based aerosol optical  
1271 depth: development and application, *Environ. Health Persp.*, 118, 847-855,  
1272 <https://doi.org/10.1289/ehp.0901623>, 2010.
- 1273 Van Donkelaar, A., Martin, R. V., Brauer, M., Hsu, N. C., Kahn, R. A., Levy, R. C., Lyapustin, A., Sayer,  
1274 A. M., and Winker, D. M.: Global estimates of fine particulate matter using a combined geophysical-  
1275 statistical method with information from satellites, models, and monitors, *Environ. Sci. Technol.*, 50,  
1276 3762-3772, <https://doi.org/10.1021/acs.est.5b05833>, 2016.
- 1277 van Donkelaar, A., Hammer, M. S., Bindle, L., Brauer, M., Brook, J. R., Garay, M. J., Hsu, N. C.,  
1278 Kalashnikova, O. V., Kahn, R. A., Lee, C., Levy, R. C., Lyapustin, A., Sayer, A. M., and Martin, R. V.:  
1279 Monthly Global Estimates of Fine Particulate Matter and Their Uncertainty, *Environ. Sci. Technol.*, 55,  
1280 15287-15300, <https://doi.org/10.1021/acs.est.1c05309>, 2021.
- 1281 Viana, M., Kuhlbusch, T. A. J., Querol, X., Alastuey, A., Harrison, R. M., Hopke, P. K., Winiwarter, W.,  
1282 Vallius, A., Szidat, S., Prevot, A. S. H., Hueglin, C., Bloemen, H., Wahlin, P., Vecchi, R., Miranda, A. I.,  
1283 Kasper-Giebl, A., Maenhaut, W., and Hitzenberger, R.: Source apportionment of particulate matter in  
1284 Europe: A review of methods and results, *J. Aerosol Sci.*, 39, 827-849,  
1285 <https://doi.org/10.1016/j.jaerosci.2008.05.007>, 2008.
- 1286 Wang, K., Dickinson, R. E., and Liang, S.: Clear Sky Visibility Has Decreased over Land Globally from  
1287 1973 to 2007, *Science*, 323, 1468-1470, <https://doi.org/10.1126/science.1167549>, 2009.
- 1288 Wang, K. C., Dickinson, R. E., Su, L., and Trenberth, K. E.: Contrasting trends of mass and optical  
1289 properties of aerosols over the Northern Hemisphere from 1992 to 2011, *Atmos. Chem. Phys.*, 12, 9387-



- 1290 9398, <https://doi.org/10.5194/acp-12-9387-2012>, 2012.
- 1291 Wang, Q., Kwan, M.-P., Zhou, K., Fan, J., Wang, Y., and Zhan, D.: The impacts of urbanization on fine  
1292 particulate matter (PM<sub>2.5</sub>) concentrations: Empirical evidence from 135 countries worldwide, *Environ.*  
1293 *Pollut.*, 247, 989-998, <https://doi.org/10.1016/j.envpol.2019.01.086>, 2019.
- 1294 Wang, Z., Li, J., Wang, Z., Yang, W., Tang, X., Ge, B., Yan, P., Zhu, L., Chen, X., Chen, H., Wand, W.,  
1295 Li, J., Liu, B., Wang, X., Wand, W., Zhao, Y., Lu, N., and Su, D.: Modeling study of regional severe hazes  
1296 over mid-eastern China in January 2013 and its implications on pollution prevention and control, *Sci.*  
1297 *China Earth Sci.*, 57, 3-13, <https://doi.org/10.1007/s11430-013-4793-0>, 2014.
- 1298 Wei, J., Li, Z., Peng, Y., and Sun, L.: MODIS Collection 6.1 aerosol optical depth products over land and  
1299 ocean: validation and comparison, *Atmos. Environ.*, 201, 428-440,  
1300 <https://doi.org/10.1016/j.atmosenv.2018.12.004>, 2019a.
- 1301 Wei, J., Huang, W., Li, Z., Xue, W., Peng, Y., Sun, L., and Cribb, M.: Estimating 1-km-resolution PM<sub>2.5</sub>  
1302 concentrations across China using the space-time random forest approach, *Remote Sens. Environ.*, 231,  
1303 <https://doi.org/10.1016/j.rse.2019.111221>, 2019b.
- 1304 Wei, J., Li, Z., Lyapustin, A., Sun, L., Peng, Y., Xue, W., Su, T., and Cribb, M.: Reconstructing 1-km-  
1305 resolution high-quality PM<sub>2.5</sub> data records from 2000 to 2018 in China: spatiotemporal variations and  
1306 policy implications, *Remote Sens. Environ.*, 252, 112136, <https://doi.org/10.1016/j.rse.2020.112136>,  
1307 2021.
- 1308 Wei, J., Li, Z., Cribb, M., Huang, W., Xue, W., Sun, L., Guo, J., Peng, Y., Li, J., and Lyapustin, A.:  
1309 Improved 1 km resolution PM<sub>2.5</sub> estimates across China using enhanced space-time extremely  
1310 randomized trees, *Atmos. Chem. Phys.*, 20, 3273-3289, <https://doi.org/10.5194/acp-20-3273-2020>,  
1311 2020a.
- 1312 Wei, J., Li, Z., Cribb, M., Huang, W., Xue, W., Sun, L., Guo, J., Peng, Y., Li, J., Lyapustin, A., Liu, L.,  
1313 Wu, H., and Song, Y.: Improved 1 km resolution PM<sub>2.5</sub> estimates across China using enhanced space-  
1314 time extremely randomized trees, *Atmos. Chem. Phys.*, 20, 3273-3289, [https://doi.org/10.5194/acp-20-](https://doi.org/10.5194/acp-20-3273-2020)  
1315 [3273-2020](https://doi.org/10.5194/acp-20-3273-2020), 2020b.
- 1316 Wu, J., Zheng, H., Zhe, F., Xie, W., and Song, J.: Study on the relationship between urbanization and fine  
1317 particulate matter (PM<sub>2.5</sub>) concentration and its implication in China, *J. Cleaner Prod.*, 182, 872-882,  
1318 <https://doi.org/10.1016/j.jclepro.2018.02.060>, 2018.
- 1319 Wu, W. and Zhang, Y.: Effects of particulate matter (PM<sub>2.5</sub>) and associated acidity on ecosystem  
1320 functioning: response of leaf litter breakdown, *Environ. Sci. Pollut. R.*, 25, 30720-30727,  
1321 <https://doi.org/10.1007/s11356-018-2922-1>, 2018.
- 1322 Xue, T., Zheng, Y., Tong, D., Zheng, B., Li, X., Zhu, T., and Zhang, Q.: Spatiotemporal continuous  
1323 estimates of PM<sub>2.5</sub> concentrations in China, 2000–2016: A machine learning method with inputs from  
1324 satellites, chemical transport model, and ground observations, *Environ. Int.*, 123, 345-357,  
1325 <https://doi.org/10.1016/j.envint.2018.11.075>, 2019.
- 1326 Yang, X., Zhao, C., Yang, Y., Yan, X., and Fan, H.: Statistical aerosol properties associated with fire  
1327 events from 2002 to 2019 and a case analysis in 2019 over Australia, *Atmos. Chem. Phys.*, 21, 3833-  
1328 3853, <https://doi.org/10.5194/acp-21-3833-2021>, 2021.
- 1329 Zeng, Z., Gui, K., Wang, Z., Luo, M., Geng, H., Ge, E., An, J., Song, X., Ning, G., and Zhai, S.:  
1330 Estimating hourly surface PM<sub>2.5</sub> concentrations across China from high-density meteorological  
1331 observations by machine learning, *Atmos. Res.*, 254, 105516,  
1332 <https://doi.org/10.1016/j.atmosres.2021.105516>, 2021.
- 1333 Zhang, Q., Zheng, Y., Tong, D., Shao, M., Wang, S., Zhang, Y., Xu, X., Wang, J., He, H., Liu, W., Ding,



1334 Y., Lei, Y., Li, J., Wang, Z., Zhang, X., Wang, Y., Cheng, J., Liu, Y., Shi, Q., Yan, L., Geng, G., Hong, C.,  
1335 Li, M., Liu, F., Zheng, B., Cao, J., Ding, A., Gao, J., Fu, Q., Huo, J., Liu, B., Liu, Z., Yang, F., He, K.,  
1336 and Hao, J.: Drivers of improved PM<sub>2.5</sub> air quality in China from 2013 to 2017, P. Natl. A.  
1337 Sci., 116, 24463-24469, <https://doi.org/10.1073/pnas.1907956116>, 2019.

1338 Zhang, S., Wu, J., Fan, W., Yang, Q., and Zhao, D.: Review of aerosol optical depth retrieval using  
1339 visibility data, Earth-Sci. Rev., 200, 102986, <https://doi.org/10.1016/j.earscirev.2019.102986>, 2020.

1340 Zhang, Z., Wu, W., Wei, J., Song, Y., Yan, X., Zhu, L., and Wang, Q.: Aerosol optical depth retrieval from  
1341 visibility in China during 1973-2014, Atmos. Environ., 171, 38-48,  
1342 <https://doi.org/10.1016/j.atmosenv.2017.09.004>, 2017.

1343 Zhao, B., Su, Y., He, S., Zhong, M., and Cui, G.: Evolution and comparative assessment of ambient air  
1344 quality standards in China, J. Integr. Environ. Sci., 13, 85-102,  
1345 <https://doi.org/10.1080/1943815X.2016.1150301>, 2016a.

1346 Zhao, S., Yu, Y., Yin, D., He, J., Liu, N., Qu, J., and Xiao, J.: Annual and diurnal variations of gaseous  
1347 and particulate pollutants in 31 provincial capital cities based on in situ air quality monitoring data from  
1348 China National Environmental Monitoring Center, Environ. Int., 86, 92-106,  
1349 <https://doi.org/10.1016/j.envint.2015.11.003>, 2016b.

1350 Zhong, J., Zhang, X., Gui, K., Liao, J., Fei, Y., Jiang, L., Guo, L., Liu, L., Che, H., and Wang, Y.:  
1351 Reconstructing 6-hourly PM 2.5 datasets from 1960 to 2020 in China, Earth Syst. Sci. Data, 14, 3197-  
1352 3211, <https://doi.org/10.5194/essd-14-3197-2022>, 2022.

1353 Zhong, J., Zhang, X., Gui, K., Wang, Y., Che, H., Shen, X., Zhang, L., Zhang, Y., Sun, J., and Zhang, W.:  
1354 Robust prediction of hourly PM<sub>2.5</sub> from meteorological data using LightGBM, Natl. Sci. Rev., 8,  
1355 nwaa307, <https://doi.org/10.1093/nsr/nwaa307>, 2021.

1356